

The High Energy X-ray Probe (HEX-P): The Future of Hard X-ray Dual AGN Science

Ryan W. Pfeifle^{1,2,†,*}, Peter G. Boorman³, Kimberly A. Weaver¹, Johannes Buchner⁴, Francesca Civano¹, Kristin Madsen¹, Daniel Stern⁵, Núria Torres-Albà⁶, Emanuele Nardini⁷, Claudio Ricci^{8,9,10}, Stefano Marchesi⁶, D. R. Ballantyne¹¹, Dominic Sicilian¹², Chien-Ting Chen^{13,14}, Elias Kammoun^{15,16,7}, Ryan C. Hickox¹⁷, Javier A. García^{1,3}, Labani Mallick^{18,19,3,†}

¹X-ray Astrophysics Laboratory, NASA Goddard Space Flight Center, Code 662, Greenbelt, MD, USA

²Oak Ridge Associated Universities, NASA NPP Program, Oak Ridge, TN, USA

[†] NASA Postdoctoral Program Fellow

³Cahill Center for Astrophysics, California Institute of Technology, 1216 East California Boulevard, Pasadena, CA 91125, USA

⁴Max Planck Institute for Extraterrestrial Physics, Giessenbachstrasse, 85748 Garching, Germany

⁵Jet Propulsion Laboratory, California Institute of Technology, Pasadena, CA, 91109, USA

⁶Department of Physics and Astronomy, Clemson University, Kinard Lab of Physics, Clemson, SC 29634, USA

⁸Instituto de Estudios Astrofísicos, Facultad de Ingeniería y Ciencias, Universidad Diego Portales, Av. Ejército Libertador 441, Santiago, Chile

⁹Kavli Institute for Astronomy and Astrophysics, Peking University, Beijing 100871, China

¹⁰George Mason University, Department of Physics and Astronomy, MS3F3, 4400 University Drive, Fairfax, VA 22030, USA

¹¹Center for Relativistic Astrophysics, School of Physics, Georgia Institute of Technology, 837 State Street, Atlanta, GA, 30332-0430, USA

¹²Department of Physics, University of Miami, Coral Gables, FL 33146

¹³Science and Technology Institute, Universities Space Research Association, Huntsville, AL 35805, USA

¹⁴Astrophysics Office, NASA Marshall Space Flight Center, ST12, Huntsville, AL 35812, USA

¹⁵IRAP, Université de Toulouse, CNRS, UPS, CNES, 9, Avenue du Colonel Roche, BP 44346, F-31028, Toulouse Cedex 4, France

¹⁶Dipartimento di Matematica e Fisica, Università Roma Tre, via della Vasca Navale 84, I-00146 Rome, Italy

¹⁷Department of Physics and Astronomy, Dartmouth College, Hanover, New Hampshire 03755, USA

¹⁸Department of Physics & Astronomy, University of Manitoba, Winnipeg, Manitoba R3T 2N2, Canada

¹⁹Canadian Institute for Theoretical Astrophysics, University of Toronto, 60 St George Street, Toronto, Ontario M5S 3H8, Canada

[†] CITA National Fellow

Correspondence*:
Ryan W. Pfeifle
ryan.w.pfeifle@nasa.gov

ABSTRACT

A fundamental goal of modern-day astrophysics is to understand the connection between supermassive black hole (SMBH) growth and galaxy evolution. Merging galaxies offer one of the most dramatic channels for galaxy evolution known, capable of driving inflows of gas into galactic nuclei, potentially fueling both star formation and central SMBH activity. Dual active galactic nuclei (dual AGNs) in late-stage mergers with nuclear pair separations < 10 kpc are thus ideal candidates to study SMBH growth along the merger sequence since they coincide with the most transformative period for galaxies. However, dual AGNs can be extremely difficult to confirm and study. Hard X-ray (> 10 keV) studies offer a relatively contamination-free tool for probing

the dense obscuring environments predicted to surround the majority of dual AGN in late-stage mergers. To date, only a handful of the brightest and closest systems have been studied at these energies due to the demanding instrumental requirements involved. We demonstrate the unique capabilities of *HEX-P* to spatially resolve the soft and - for the first time - hard X-ray counterparts of closely-separated ($\sim 2'' - 5''$) dual AGNs in the local Universe. By incorporating state-of-the-art physical torus models, we reproduce realistic broadband X-ray spectra expected for deeply embedded accreting SMBHs. Hard X-ray spatially resolved observations of dual AGNs – accessible only to *HEX-P* – will hence transform our understanding of dual AGN in the nearby Universe.

Keywords: Dual AGN, Galaxy Merger, X-ray Astronomy, Active Galactic Nucleus, Galaxy Interaction

1 INTRODUCTION

It has long been known that galaxy interactions and mergers give rise to gravitational torques that can transform the structure and composition of the constituent galaxies (e.g., Toomre and Toomre, 1972). These torques can funnel vast quantities of gas into the central nuclei of the galaxies (e.g., Barnes and Hernquist, 1991, 1996), creating reservoirs that can then fuel star formation as well as the central supermassive black holes (SMBHs), which ignite as active galactic nuclei (AGNs) (Hopkins et al., 2006, 2008). A natural product of galaxy mergers are dual AGNs, that is, synchronized SMBH growth in both galaxies (Van Wassenhove et al., 2012). Simulations of galaxy mergers predict that the growth of the central SMBHs is better synchronized in the latest stages of the merger sequence, when the central nuclei are separated by $\lesssim 10$ kpc (Van Wassenhove et al., 2012; Capelo et al., 2015; Blecha et al., 2018), though dual AGNs can be found across the full merger sequence, from separations below 1 kpc (e.g., Komossa et al., 2003; Koss et al., 2023) and up ~ 50 kpc or more (Liu et al., 2011; Koss et al., 2012; De Rosa et al., 2018, 2023), and the synchronized activation of a dual AGN is a strong function of progenitor mass ratios, morphological types, gas masses, and radiative feedback (e.g., Callegari et al., 2009, 2011; Van Wassenhove et al., 2012; Capelo et al., 2015; Blecha et al., 2018; Li et al., 2021). Dual AGNs represent a potentially important phase of SMBH growth: they are predicted to be heavily obscured across the merger sequence (Blecha et al., 2018) and in late-stage mergers they are expected to coincide with the most obscured and expeditious growth of the two SMBHs (Blecha et al., 2018; Capelo et al., 2015). These predictions find support in observations showing that, relative to mass- and redshift-matched control galaxies, the AGN fraction in galaxy mergers increases with decreasing nuclear pair separation (Ellison et al., 2011; Satyapal et al., 2014; Weston et al., 2017), where the increase in AGN fraction is most dramatic when selecting AGNs based on mid-IR colors (Satyapal et al., 2014; Weston et al., 2017). A large fraction of known dual AGNs show evidence for heavy obscuration (see Section 5.2 in Pfeifle et al., 2023) which is consistent with theoretical predictions, but such evidence is admittedly still relatively circumstantial and may depend upon selection method; statistically complete studies of dual AGNs are still needed. Nonetheless, with additional evidence of dramatic AGN feedback in known dual AGNs (Müller-Sánchez et al., 2018), dual AGNs in late-stage mergers may represent one of the most transformative phases of the entire merger sequence for both the SMBHs and their hosts. Dual AGNs also represent the observational forerunner to gravitationally-bound binary SMBHs, the inspiral and coalescence of which will emit the most titanic of gravitational wave signals (GW) and will be accessible to future space-based GW facilities (e.g., LISA, Amaro-Seoane et al., 2023, which will be sensitive to intermediate-mass black hole binaries). Despite this presumed importance, dual AGNs have remained relatively elusive, and a variety of selection strategies have been pursued to uncover them: optical spectroscopic emission line ratios Liu et al. (2011), double-peaked emission lines

(e.g., Zhou et al., 2004; Wang et al., 2009; Liu et al., 2010; Smith et al., 2010; Comerford et al., 2011, 2012; Ge et al., 2012), infrared colors (Imanishi and Saito, 2014; Satyapal et al., 2017; Ellison et al., 2017; Pfeifle et al., 2019b,a; Imanishi et al., 2020; Barrows et al., 2023), hard X-ray selection (Koss et al., 2012), and most recently varstrometry (Hwang et al., 2020; Shen et al., 2021; Schwartzman et al., 2023) and Gaia multi-source strategies (Shen et al., 2019; Mannucci et al., 2022; Ciurlo et al., 2023). Serendipitous (e.g., Komossa et al., 2003; Guainazzi et al., 2005; Piconcelli et al., 2010) and follow-up X-ray observations (Bianchi et al., 2008; Comerford et al., 2011; Koss et al., 2012; Liu et al., 2013; Comerford et al., 2015; Satyapal et al., 2017; Pfeifle et al., 2019b,a; Hou et al., 2019; Gross et al., 2019; Hou et al., 2020, 2023) are a common method by which dual AGNs are confirmed¹, particularly in cases where dual AGNs cannot be selected through common optical diagnostics (e.g., NGC 6240, Komossa et al., 2003). These investigations have revealed a prevalence of high column densities in the known population of dual AGNs (e.g., Komossa et al., 2003; Bianchi et al., 2008; Piconcelli et al., 2010; Ptak et al., 2015; Nardini, 2017; De Rosa et al., 2018; Pfeifle et al., 2019b,a; De Rosa et al., 2023); see discussion in Pfeifle et al. (2023).

While *Chandra* and *XMM-Newton* have been used effectively in the past to identify, confirm, and/or characterize dual AGN systems, their soft X-ray bandpasses (0.5 – 10 keV) bias them against detecting and properly characterizing the X-ray spectral properties and the circumnuclear obscurers in heavily obscured dual AGNs with column densities $N_{\text{H}} > 5 \times 10^{23} - 10^{24} \text{ cm}^{-2}$, as predicted (Hopkins et al., 2008; Capelo et al., 2015, 2017; Blecha et al., 2018) and observed (e.g., Komossa et al., 2003; Ballo et al., 2004; Bianchi et al., 2008; Mazzarella et al., 2012; Koss et al., 2016; De Rosa et al., 2018; Iwasawa et al., 2018; Pfeifle et al., 2019a; Guainazzi et al., 2021; Iwasawa et al., 2020; De Rosa et al., 2023), particularly in late-stage mergers (e.g., Ricci et al., 2017, 2021). In fact, this is a particular concern in LIRGs and ULIRGs; though the statistics are small, a higher fraction of dual AGNs were identified among the lower IR luminosity GOALS sample (Torres-Albà et al., 2018) than the brighter IR luminosity sample (Iwasawa et al., 2011), which can possibly be interpreted as the dual AGNs in the high luminosity sample being too obscured for *XMM-Newton* or *Chandra* to detect and too close together to be resolved by *NuSTAR* (Torres-Albà et al., 2018). Hard X-ray bandpasses ($> 10 \text{ keV}$), on the other hand, provide access to harder X-ray features, such as Compton reflection, that are vital for providing accurate constraints on the X-ray properties of heavily obscured AGNs. *NuSTAR*, with its sensitivity over the 3–78 keV bandpass, has detected and studied the hard X-ray dual AGN counterparts (when present) in Arp 299 (though only one of the dual AGNs was detected, Ptak et al., 2015, but see Section 5 below), ESO 509-IG066 (Kosec et al., 2017), MCG+04-48-002/NGC 6921 (Koss et al., 2016), and NGC 833/NGC 835 Oda et al. (2018), all of which are local, relatively bright, and have separations large enough for *NuSTAR* to spatially resolve ($\sim 16'' - 91''$, though at $16''$ the two sources would appear as a convolved, elongated single source). However, hard X-ray observations of dual AGNs with *NuSTAR* are relatively uncommon, and most dual AGN studies performed with *NuSTAR* suffer from non-detections due to *NuSTAR*'s sensitivity limit (e.g., Ptak et al., 2015; Ricci et al., 2017; Pfeifle et al., 2023) and/or convolved sources due to *NuSTAR*'s angular resolution (HPD $\sim 58''$, $18''$ FWHM; Yamada et al., 2018; Iwasawa et al., 2018; Pfeifle et al., 2019a; Iwasawa et al., 2020; Pfeifle et al., 2023). This requires a great deal of care and caution when performing the spectroscopic analysis and interpreting the results (e.g., the case of NGC 6240, Nardini, 2017). To usher in revolutionary advances in hard X-ray dual AGN science, new facilities with higher spatial resolution and greater sensitivity at hard X-ray energies ($> 10 \text{ keV}$) are required.

¹ Radio imaging is also an effective method of selecting (Fu et al., 2015a) as well as confirming or rejecting dual AGN candidates (e.g., Fu et al., 2011; Gabányi et al., 2014; Frey et al., 2012; Gabányi et al., 2016; Fu et al., 2015b; Müller-Sánchez et al., 2015; Rubinur et al., 2019).

In this paper, we discuss the feasibility of hard X-ray dual AGN science with the High Energy X-ray Probe (HEX-P) mission concept. The current mission design for *HEX-P* is described in Section 2. In Section 3 we describe our *HEX-P* imaging and spectroscopic simulations, generated using the SOXS (ZuHone et al., 2023) and SIXTE (Dauser et al., 2019) software packages. We outline the potential for resolving hard and soft X-ray signatures from dual AGNs with *HEX-P* using the instrument and facility design described in Section 4.1, the feasibility of using nested sampling and Bayesian statistical source detection techniques to probe closely-separated hard X-ray sources in Section 4.1, and we compare these results to what is currently possible with *NuSTAR* in Section 4.2. In Section 5, we examine simulated hard X-ray imaging and spectra for the dual AGN in Arp 299 as a test case for *HEX-P* dual AGN science, wherein we use state-of-the-art torus models and Bayesian fitting techniques to constrain the line-of-sight column densities, photon indices, and other spectroscopic parameters of the AGNs. We discuss the issue of spectral contamination for closely separated sources in Section 6. In Section 7 we briefly outline synergies with upcoming ground-based and space-based facilities. We provide concluding remarks in Section 8

2 MISSION DESIGN

The *HEX-P* (Madsen et al. 2023, in preparation) is a probe-class mission concept that offers sensitive broad-band spectral coverage (0.2–80 keV) with exceptional spectral, timing and angular capabilities. It features two high-energy telescopes (HETs) that focus hard X-rays, and one low-energy telescope (LET) that focuses lower energy X-rays.

The LET consists of a segmented mirror assembly coated with Ir on monocrystalline silicon that achieves a half power diameter of 3.5", and a low-energy DEPFET detector, of the same type as the Wide Field Imager (WFI; Meidinger et al., 2020) onboard Athena (Nandra et al., 2013). It has 512 x 512 pixels that cover a field of view of 11.3' x 11.3'. It has an effective passband of 0.2–25 keV, and a full frame readout time of 2 ms, which can be operated in a 128 and 64 channel window mode for higher count-rates to mitigate pile-up and faster readout. Pile-up effects remain below an acceptable limit of $\sim 1\%$ for a flux up to ~ 100 mCrab (2–10 keV) in the smallest window configuration. Excising the core of the PSF, a common practice in X-ray astronomy, will allow for observations of brighter sources, with a typical loss of up to $\sim 60\%$ of the total photon counts.

The HET consists of two co-aligned telescopes and detector modules. The optics are made of Ni-electroformed full shell mirror substrates, leveraging the heritage of XMM-Newton (Jansen et al., 2001), and coated with Pt/C and W/Si multilayers for an effective passband of 2–80 keV. The high-energy detectors are of the same type as flown on *NuSTAR* (Harrison et al., 2013), and they consist of 16 CZT sensors per focal plane, tiled 4 x 4, for a total of 128 x 128 pixel spanning a field of view slightly larger than for the LET, 13.4'x13.4'.

The broad X-ray passband and superior sensitivity will provide a unique opportunity to study dual AGNs and galaxy mergers across a wide range of energies, luminosity ratios, pair separations, and dynamical regimes.

All the simulations presented here were produced with a set of response files that represent the observatory performance based on current best estimates as of Spring 2023 (see Madsen+23). The effective area is derived from ray-tracing calculations for the mirror design including obscuration by all known structures. The detector responses are based on simulations performed by the respective hardware groups, with an optical blocking filter for the LET and a Be window and thermal insulation for the HET. The LET background was derived from a GEANT4 simulation (Eraerds et al., 2021) of the WFI instrument, and the

HET backgrounds was derived from a GEANT4 simulation of the *NuSTAR* instrument. Both simulations adopt the L1 orbit for HEX-P.

3 SIMULATING DUAL AGNS USING SOXS AND SIXTE

To simulate *HEX-P* observations of dual AGNs, we rely upon two software suites: (1) the SIMULATED OBSERVATIONS OF X-RAY SOURCES (SOXS, ZuHone et al., 2023) suite, to create the SIMULATED inPUT (SIMPOT) files that store the spatial and spectral models used for the simulations, and (2) the SIMULATION OF X-RAY TELESCOPES (SIXTE, Dauser et al., 2019) suite, which was used to generate the actual simulated observations.

Each simulation includes two AGNs represented as point source spatial models (hereafter AGN 1 and AGN 2), and we produced simulations for a variety of separations, ranging from 50'' down to 20'' in increments of 10'' as well as from 20'' down to 0'' in increments of 2''. Here, the 0'' case represents the “null” expectation of what a single source would look like at the combined flux level of the AGNs in our simulations and it is included for visual comparison purposes. For illustrative purposes in this work, we also include simulations of AGNs separated by 15'', 5'', 3'', and 1''. We use the following components to develop the spectral models for the AGNs: (1) an absorbed power law ($\Gamma = 1.8$) that accounts for photoelectric absorption and Compton scattering; (2) reprocessed emission from a torus (BORUS, Baloković et al., 2018, which self consistently accounts for absorption, fluorescence, and Compton scattering for a toroidal distribution of obscuring gas); (3) two soft X-ray thermal components (APEC) to model emission due to star formation, motivated by the common presence of soft thermal components in many dual AGNs and candidate systems (see, e.g., Section 5.4 in Pfeifle et al., 2023); (4) a power law to model Thomson scattering (0.5%). This AGN spectroscopic model is described in XSPEC as:

$$tbabs \times (borus + ztbabs \times cabs \times cutoffpl + const \times cutoffpl + apec + apec) \quad (1)$$

Each AGN spectrum is simulated at a redshift of $z = 0.05$ ($D_L = 222.3$ Mpc). We assume an approximately edge-on torus viewing angle of $\theta_{\text{view}} = 70^\circ$ and a covering factor of $C = 85\%$; this latter assumption is motivated by the expectation that mergers should result in heavily obscured AGNs with high covering factors (Ricci et al., 2017). AGNs 1 and 2 have observed (uncorrected for intrinsic absorption) 2 – 10 keV fluxes normalized to 1.0×10^{-13} and 5.0×10^{-14} erg cm $^{-2}$ s $^{-1}$, respectively. For each choice of separation, we run the spectral model of each AGN over a small list of line-of-sight column densities, $\log(N_{\text{H}}/\text{cm}^2) = 22, 23, 24$ (for simplicity we assume the average torus column density and the line-of-sight column density are equal); we therefore end up with nine SIMPUT files for each separation, where each SIMPUT file probes a separate pairing in terms of obscuration; i.e., one Compton-thick ($N_{\text{H}} > 10^{24}$ cm $^{-2}$) pair, four Compton-thick and Compton-thin ($N_{\text{H}} < 10^{24}$ cm $^{-2}$) pairs, and four Compton-thin-Compton-thin pairs. SOXS is then used to convolve the spatial and spectral models to produce the SIMPUT files for each AGN pairing.

Each SIMPUT file generated above was fed to SIXTE in order to generate the *HEX-P* HET and LET event files. For each AGN pairing, we assumed a 50 ks exposure (which could be the typical exposure time in the *HEX-P* wide area survey, and is also similar in length to archival *NuSTAR* observations of dual AGNs, i.e., $\sim 20 - 60$ ks) and generated event files for HET 1, HET 2, an effective (co-added) 2-camera HET event file, and a LET event file using the v7 *HEX-P* response files (see Madsen et al. 2023). Science images were generated for all three *HEX-P* cameras using the IMGEV command and spectra were extracted using the MAKESPEC command from 10'' apertures (unless states otherwise in the text) centered on the AGN

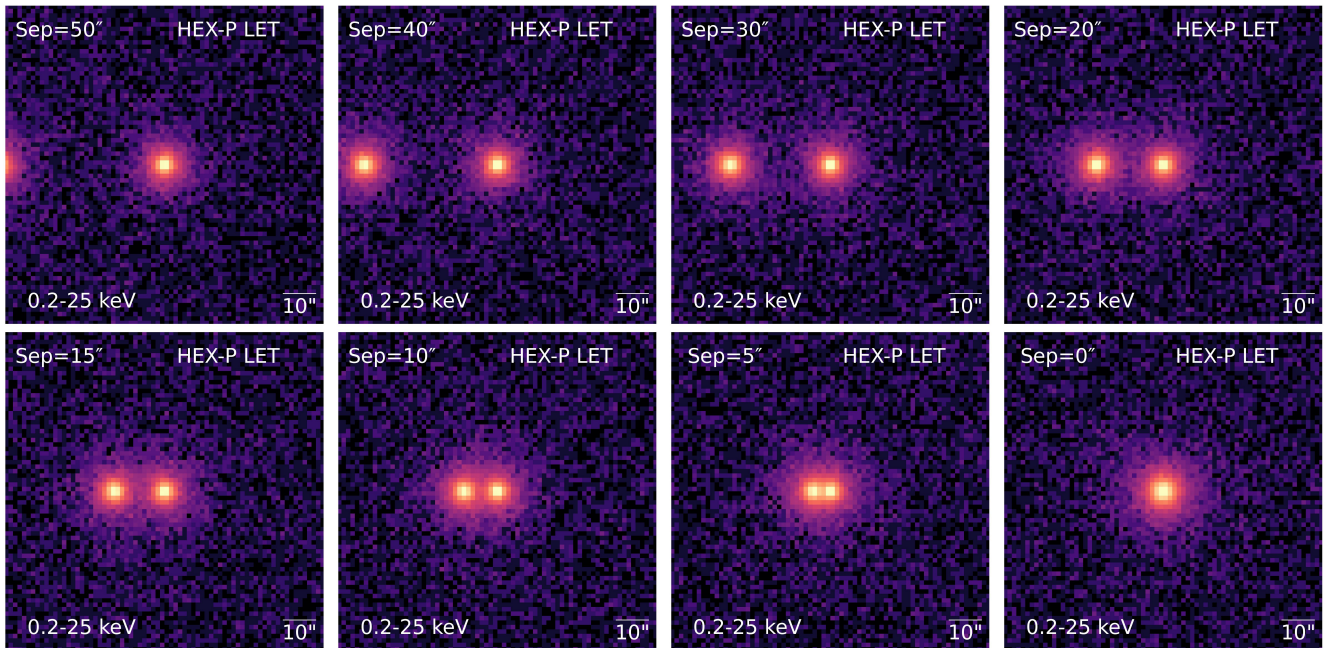


Figure 1. This 8-panel figure shows the LET 0.2-25 keV 50 ks images (1-pixel smoothing). Panels represent angular separations ranging from 50'' down to 0''. The two AGNs are distinguishable by eye down to 5'' and can be identified using Bayesian detection methods (see Section 4.1) down to separations of $\sim 2''$. The “null” case of 0'' (representing a single AGN at the combined flux level of our sources) is included for visual comparison. The AGNs have observed 2-10 fluxes of 1.0×10^{-13} and 5.0×10^{-14} erg cm $^{-2}$ s $^{-1}$. These panels display the case in which both AGNs are Compton-thick, though the Compton-thick/Compton-thin and Compton-thin/Compton-thin cases show similar X-ray morphologies.

positions. We performed the same set of commands in SIXTE for the analogous *NuSTAR* simulated imaging using the *NuSTAR* response files² and a background file derived from the COSMOS field (Civano et al., 2015).

4 HARD X-RAY IMAGING RESULTS FOR DUAL AGNS

4.1 HEX-P HET and LET Imaging of Dual AGNs

We show a subset of our dual AGN simulation suite in Figure 1 and Figure 2 for the 0.2-25 keV LET and (co-added two-camera) 2-80 keV HET imaging, respectively, with each panel representing a distinct pair separation, ranging from 50'' down to 0'' in 10'' or 5'' intervals. AGN 1 (centered in the field of view) is clearly seen in the center of each panel, while AGN 2 can be seen moving closer in from the left with each successive panel. These images clearly show the two AGNs are distinguishable by eye down to $\sim 5''$ in both the HET and LET; we include a finer grid of separations in the Appendix with separations ranging from 5'' down to 1'' in 1'' intervals, which demonstrates that the AGNs can be distinguished by eye even down to $\sim 4''$ in HET imaging and $\sim 3''$ in LET imaging.

Probing dual AGNs with *HEX-P* down to separations $\lesssim 5''$ is a particularly important task, as dual AGNs are predicted to experience the peak of their merger-driven luminosities and obscuration in late-stage mergers (Capelo et al., 2015; Blecha et al., 2018) when the nuclei of the galaxies are separated

² https://www.nustar.caltech.edu/page/response_files

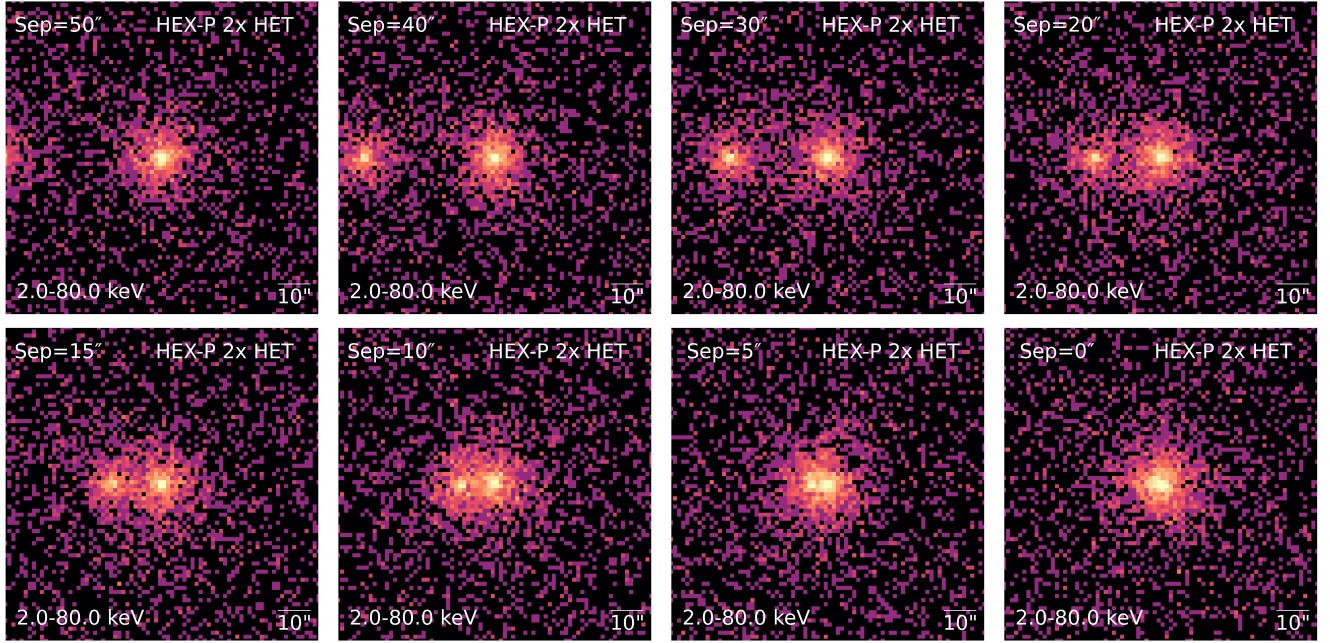


Figure 2. This 8-panel figure shows the effective 2-camera HET 2-80 keV, 50 ks images (1-pixel smoothing). As in Figure 1, panels represent angular separations ranging from 50'' down to 0''. The two AGNs are distinguishable by eye down to 5'' and can be identified using Bayesian detection methods (see Section 4.1 down to separations of $\sim 2''$). The AGNs have observed 2-10 fluxes of 1.0×10^{-13} and 5.0×10^{-14} erg cm $^{-2}$ s $^{-1}$. These panels display the case in which both AGNs are Compton-thick, though the Compton-thick/Compton-thin and Compton-thin/Compton-thin cases show similar X-ray morphologies.

by $\lesssim 10$ kpc ($\lesssim 10.2''$ at $z = 0.05$). *HEX-P*'s access to X-ray energies beyond 10 keV will be vital to constraining the intrinsic luminosities and distinct column densities along the line-of-sight to each AGN in a merging system, an impossibility with *NuSTAR* for all but the nearest and brightest (Nardini, 2017) and/or most widely-separated dual AGNs known (e.g., Ptak et al., 2015; Kosec et al., 2017; Oda et al., 2018). Furthermore, broadband coverage is fundamental not only to detect obscured AGN, but also to characterize their obscuration without biases; broadband hard X-ray coverage with *NuSTAR*, for example, has led to dramatic refinements in AGN column density estimates compared to constraints derived from only soft X-ray or joint soft and ultra-hard X-ray coverage (e.g., Marchesi et al., 2018, 2019). Here we discuss the possibility of probing dual AGNs with separations $1'' < r_p < 5''$ in the hard X-rays with *HEX-P*.

We analyse each simulated event file with a single and double point source model, with wide, uninformative priors on the location and the total counts of each point source, I . The first point source is assumed to be located near the image centre ± 10 px. Both models also include a background count rate, B , that is constant across the image and left free during the fit. A standard Poisson likelihood is used, with the symmetric PSF model $\text{PSF}(\Delta r)$ extracted from simulations:

$$\mathcal{L} \propto \frac{\prod_{i \in \text{events}} M(x_i, y_i | x_c, y_c, I, B)}{\int \int M(x_i, y_i | x_c, y_c, I, B) dx dy} \quad (2)$$

For the single point source model,

$$M(x, y | x_c, y_c, I, B) = I \times \text{PSF} \left(\sqrt{(x_i - x_c)^2 + (y_i - y_c)^2} \right) + B \quad (3)$$

while for the two point source model there are two centres and intensities.

The Akaike Information Criterion (AIC; Akaike 1974) of the two models is compared to determine whether the single or double source model is preferred. In order for this comparison to take place, we first calibrated our detection algorithm using simulations of convolved X-ray sources, where we simulated two co-spatial X-ray sources with identical fluxes to those in our AGN simulations described in Section 3. We simulated 100 cases of convolved sources for the LET as well as for the HET×2, ran the detection algorithm on each case, and recorded the resulting AIC values. This calibration set the baseline for an acceptable AIC threshold to differentiate between a single and dual source case. We are able to detect X-ray point sources in both the LET 0.2-25 keV bandpass and the HET 2-80 keV bandpass down to separations of 2". This result comes with the caveat that this detection routine is a proof-of-concept and the results are subject to change based on the exposure time and the fluxes of the sources: all else being equal, we cannot necessarily differentiate between multiple sources at 2" or 3" separations for lower exposure times; alternatively, we can probe down to closer pair separations (< 2") for higher flux levels (a more rigorous examination is left to future works). Nonetheless, this is essentially an order-of-magnitude improvement over current capabilities with *NuSTAR*.

While dual AGNs are predicted to be heavily obscured in late-stage mergers (Blecha et al., 2018), there are cases of heavily obscured dual AGNs in widely-separated merging pairs of galaxies (Koss et al., 2012; De Rosa et al., 2018, 2023). Given that dual AGNs are also predicted to become heavily obscured after only the second pericenter passage (Blecha et al., 2018), and that AGNs are expected to flicker on and off across the merger sequence (e.g., the AGN duty cycle << the merger timescale Schawinski et al., 2015; Goulding et al., 2019), *HEX-P* may reveal multi-modal distributions of heavily obscured AGNs across the merger sequence, rather than only during the latest stages of the merger sequence.

4.2 A Substantial Improvement over *NuSTAR*

In an analogous fashion to the *HEX-P* simulated event files displayed in Figures 1 and 2, we have used identical input models, exposure times, and separations to develop *NuSTAR* dual AGN imaging that incorporates the *NuSTAR* background derived from the COSMOS field (Civano et al., 2015). Figure 3 displays these simulated *NuSTAR* images (where the color scale matches that of the HET imaging in Figure 2), in which the positions of the AGNs are denoted with black crosses; AGN 1 can be seen in a few (but not all) of the panels above the background while AGN 2 is virtually imperceptible in almost every panel. This figure clearly illustrates that - at these realistic observed flux levels of 1×10^{-13} and 5×10^{-14} erg cm⁻² s⁻¹ - *NuSTAR* cannot reliably identify dual AGNs in these pairings; it is important to note that dual AGNs separated by ~ 20" and 0" are essentially indistinguishable, emphasizing that *NuSTAR* cannot be used to reliably resolve < 20" dual AGNs. *HEX-P*, on the other hand, can spatially resolve each AGN in both the HET and LET imaging down to separations of ~ 5" (and ~ 2" when rigorous detection algorithms are used; see Section 4.1); this is a substantial improvement over *NuSTAR* and emphasizes that the future of hard X-ray dual AGN science relies critically upon access to facilities such as *HEX-P*.

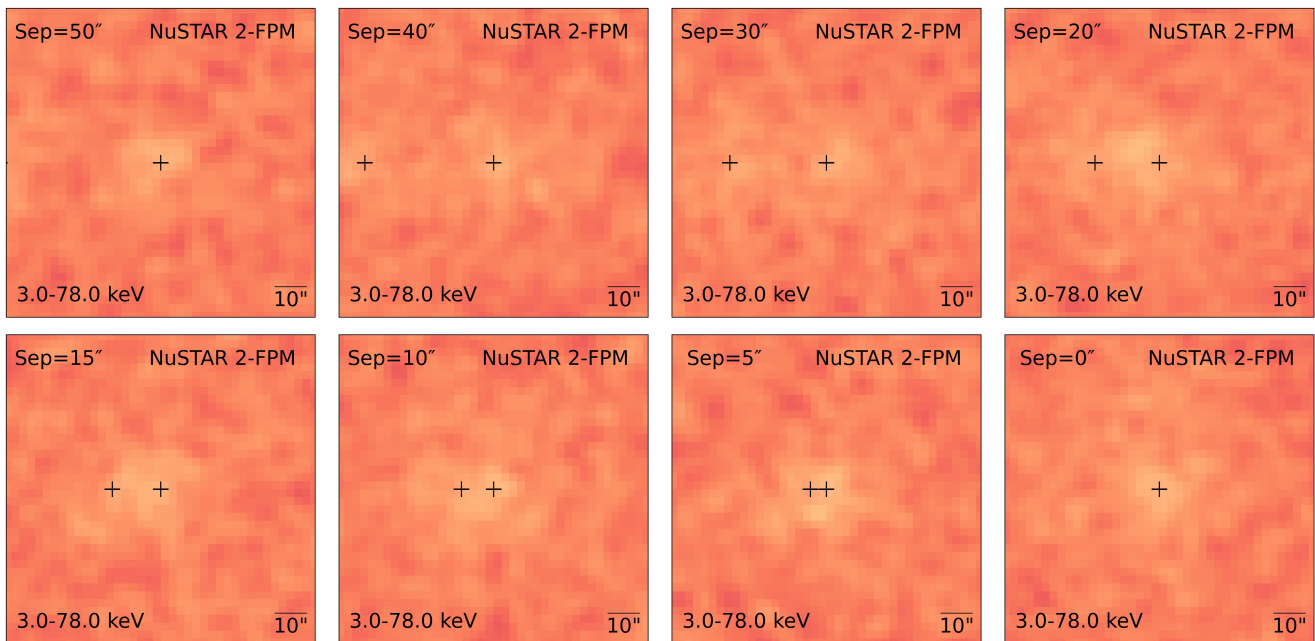


Figure 3. This 8-panel figure shows simulated two-camera 3-78 keV FPMA+B 50 ks imaging with *NuSTAR* for the same suite of dual AGNs described in Section 3. The suite of AGNs range in separation from 50'' down to 0''; the scale bar in the bottom right corner of each panel indicates an angular scale of 10''. These panels use the same scaling as in Figure 1 for the *HEX-P* HET 2-80 keV imaging. The primary AGN can be seen above the background, but the weaker secondary AGN is essentially imperceptible above the background in all of the panels. Black markers are included to denote the positions of the two AGNs.

4.3 A Substantial Improvement over Soft X-ray Missions

In Figure 4 we display a simulated 50 ks *Chandra* 2-8 keV image alongside the 2-25 keV LET and 2-80 keV HET \times 2 imaging for the case where the AGNs are separated by 10''. While *Chandra* can clearly resolve two X-ray cores emitted by the AGNs at > 2 keV, the detections are obviously limited to energies < 8 keV. To offer a quantitative comparison between *Chandra* and *HEX-P*, we extracted (background subtracted) counts for each AGN in the *Chandra*, LET, and HET imaging. The AGNs are detected with 175 ± 14 counts (AGN 1) and 67 ± 9 counts (AGN 2) in the 2-8 keV *Chandra* band when using 3'' extraction apertures ($\sim 100\%$ EEF); it is important to note that most dual AGNs and candidates are observed for < 30 ks, so with a more realistic exposure time these sources would only have been detected with $\lesssim 100$ and $\lesssim 40$ counts. Contrasting this with the detections in LET, we detect 215 ± 16 and 129 ± 13 counts in the LET 2-25 keV band for the two AGNs when using 3.5'' extraction apertures ($\sim 50\%$ EEF). At this separation, the two AGNs begin to severely contaminate one another in the HET imaging when using 8.5'' (50% EEF) apertures, so we instead excise only the inner 3.5'' of each hard X-ray source (20-25% EEF): we find the two AGNs are detected in the HET with 278 ± 17 and 189 ± 14 counts in the 2-80 keV band; these comparisons demonstrate that, given the same exposure time, *HEX-P* offers comparable, if not superior, photometric analyses on top of access to the hard X-rays.

To compare the spectroscopic capabilities of *HEX-P* to *Chandra*, we extracted the spectrum of the weaker of the two AGNs (AGN 2) from the *Chandra* and *HEX-P* images using a 3'' aperture for the *Chandra* image, a 3.5'' aperture for LET, and a 3.5'' aperture in HET \times 2; these apertures represent the $\sim 100\%$, $\sim 50\%$, and 22% EEF for each instrument. This comparison therefore represents the “best-case” scenario

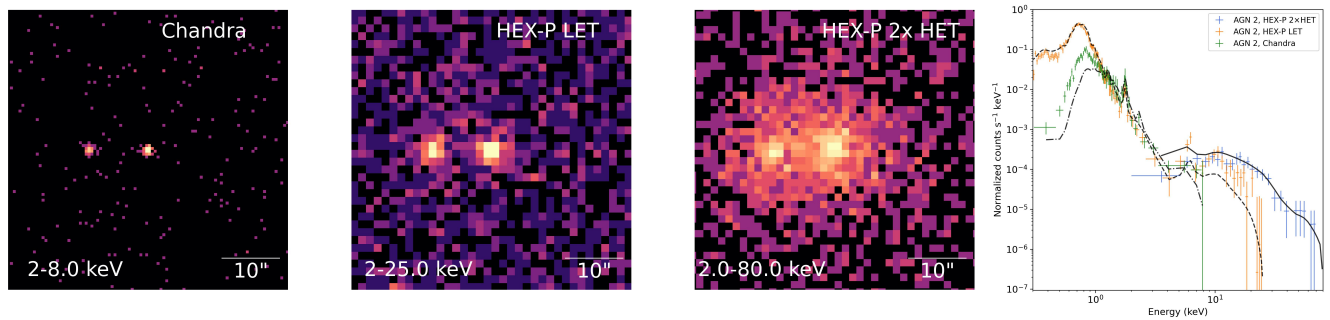


Figure 4. This four-panel figure shows a comparison between simulated *Chandra*, *HEX-P* LET, and *HEX-P* HET imaging and spectroscopy. The three X-ray imaging panels show the *Chandra* 2–8 keV, *HEX-P* LET 2–25 keV, and *HEX-P* 2–80 keV energy bands. The fourth panel displays the extracted *Chandra* (green) and *HEX-P* LET (orange) and HET (blue) spectra for AGN 2 (the weaker of the two AGNs, see Section 3), binned at 5σ .

for a *Chandra* exposure, a “standard case” for a LET exposure, and a “poor case” scenario for HET \times 2. The spectra (*Chandra*: green points, LET: orange points, HET \times 2: blue points) are shown in the fourth panel of Figure 4 and binned at 3σ per bin for visualization purposes. Only LET and HET can access energies beyond 10 keV, where HET can reach out even to 80 keV. The Compton-hump beyond 10 keV is a spectral feature critical for accurate constraints on the line-of-sight absorbing columns (e.g., P. G. Boorman, in preparation), and it is clearly accessible to the HET. The Fe K α emission line is another crucial spectral imprint of cold reflection, and a simple fit using a phenomenological power law model reveals that the addition of a Gaussian emission line to account for Fe K α does not statistically improve the fit to the simulated *Chandra* spectrum, but it *does* statistically improve the fit to the LET spectrum. Thus, this case study illustrates clearly that *HEX-P* can simultaneously access two AGN reflection features important for accurate column density constraints that would, in this case, be inaccessible to soft X-ray missions. It is important to note, too, that while soft X-ray missions can in principle detect the Fe K α emission line, intrinsic parameter estimations (including column density determination) can still be degenerate when using the Fe K α emission line alone (e.g., LaMassa et al., 2017) without harder X-ray features, whereas constraints that use the Fe K α line and the Compton-hump in tandem offer clearer and more reliable constraints (e.g., LaMassa et al., 2019). Without simultaneous access to these X-ray spectral features, soft X-ray missions will continue to be at a disadvantage when it comes to answering open questions related to dual AGN obscuration and fueling in the X-rays.

4.4 Hard X-ray Dual AGN Science as a Function of Redshift

Current hard X-ray facilities (e.g., *NuSTAR*) limit the study of distinct AGNs within dual AGN pairings to only the nearest, brightest, and/or more widely-separated systems. Figure 5 shows the distribution of angular separations for optical dual AGN candidates from Liu et al. (2011) as a function of redshift out to $z \sim 0.3$. The overlaid black dash-dotted line indicates the angular resolution of *NuSTAR* (18'' FWHM, 58'' HPD, Harrison et al., 2013), while the red dashed, dash-dotted, and dotted curves indicate nuclear pair separations of 30, 20, and 10 kpc. Overlaid on this figure, we have also plotted the corresponding *HEX-P* 2–10 keV luminosity limits (vertical dotted, black lines) as a function of redshift, informed by the limiting flux of 3.8×10^{-14} erg cm $^{-2}$ s $^{-1}$ for a 50 ks exposure; the vast majority of dual AGNs have 2–10 keV luminosities $\lesssim 10^{43}$ erg s $^{-1}$. Therefore, $z \approx 0.3$ is an approximate redshift limit for dual AGN studies with *HEX-P*. Even late-stage mergers ($\lesssim 10$ kpc) become virtually inaccessible to *NuSTAR* already

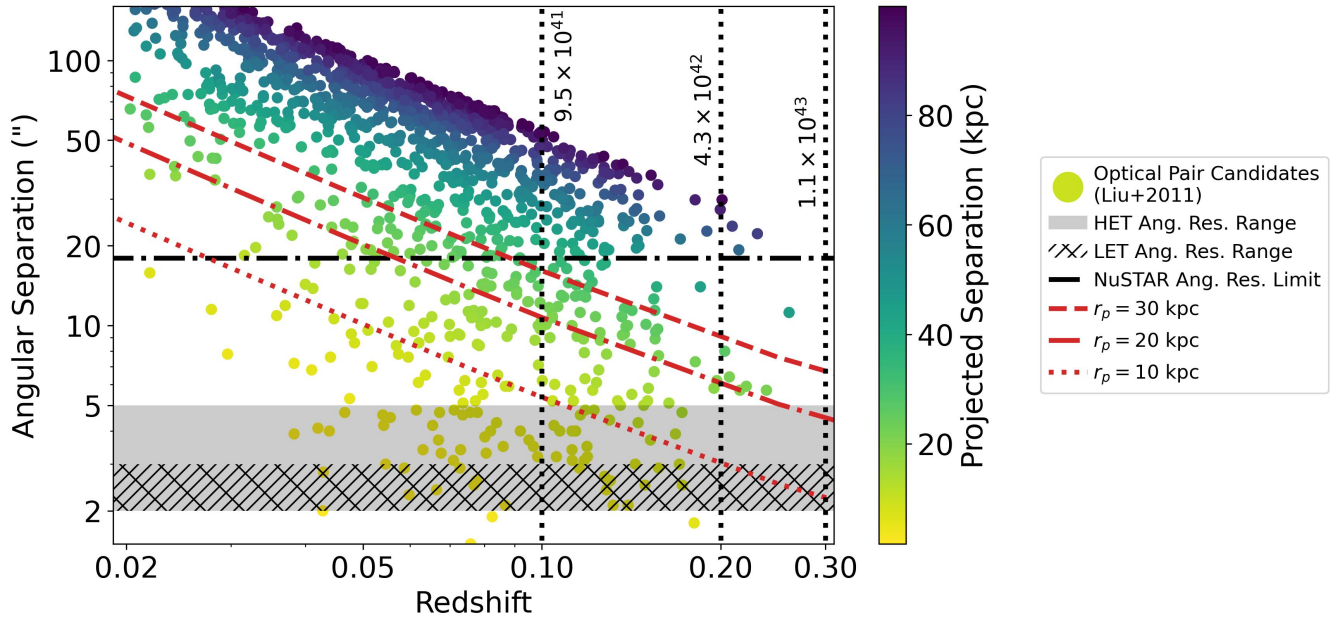


Figure 5. Redshift vs. angular separation. We have plotted the sample of optical dual AGN candidates from Liu et al. (2011) at $z < 0.3$. Markers are color coded according to the projected separation of the pair (given on the auxiliary axis). Red dashed, dash dotted, and dotted lines indicate projected separations of 30, 20, and 10 kpc. The grey, shaded region indicates the HET angular resolution limits when examining sources visually by eye ($\sim 5''$) and when using Bayesian detection algorithms ($\sim 2''$, see Section 4.1); the hashed and shaded region similarly indicates the LET angular resolution limits ($\sim 3''$ by eye, $\sim 2''$ using Bayesian detection routines). The angular resolution limits derived via the Bayesian detection algorithm in Section 4.1 are subject to change based upon the exposure time and source fluxes; here they refer specifically to the 50 ks exposure time and source fluxes listed in Section 3. *NuSTAR*'s angular resolution limit ($18''$ PSF, Harrison et al., 2013) is denoted with a dashed-dotted black line. Vertical, dotted lines denote the observed 2–10 keV AGN luminosity that corresponds to the *HEX-P* flux sensitivity limit of $3.8 \times 10^{-14} \text{ erg cm}^{-2} \text{ s}^{-1}$ in a 50 ks exposure (signal-to-noise of 5).

by $z \approx 0.025$, and more widely separated pairs (~ 30 kpc) become inaccessible by only $z \approx 0.09$. *HEX-P*, on the other hand, thanks to resolving separations of $\sim 5''$ (possibly even $\sim 2''$), can distinguish AGNs in late-stage mergers out to redshifts of $z \sim 0.1$ (or even $z \sim 0.2$ with Bayesian analyses, Section 4.1) and can access distinct AGNs in ~ 30 kpc-separated duals out to $z \sim 0.3$. Though *distinct* AGNs within late-stage mergers will not be probed beyond $z \sim 0.1 - 0.2$, *HEX-P* will be able to probe the ‘gross’ X-ray properties of these systems³; even when unresolved, *HEX-P* is required to probe the Compton hump and understand the circumstances of the nuclear environment properly, which cannot be done using soft X-ray, optical, near-IR, or radio observations. *HEX-P* will probe distinct AGNs in early-stage mergers well beyond $z \sim 0.1$ and aid in our understanding of dual AGN activation and obscuration across the merger sequence.

5 A TEST CASE FOR HEX-P: ARP 299

One illustrative case study for examining the effectiveness of *HEX-P* over *NuSTAR*, in terms of spectroscopic and imaging constraints, is Arp 299, a local (44 Mpc, or $z \sim 0.01$) dual AGN comprising an X-ray bright

³ Selected presumably in the soft X-rays with *Chandra*, via high-resolution radio imaging, space-based high-resolution optical or near-IR spectroscopy (e.g., Hubble Space Telescope or JWST), or via ground-based adaptive-optics-assisted optical or near-IR observations. However, some fraction of dual AGNs will be missed at optical wavelengths (e.g., Koss et al., 2012) and require the detection of distinct X-ray AGNs for unambiguous confirmation.

and heavily obscured AGN in the southwest nucleus (Arp 299-B, detected by *Chandra* and *NuSTAR*, Ballo et al., 2004; Ptak et al., 2015) and an AGN in the northeast nucleus (Arp 299-A) identified as a flat spectrum radio source (Pérez-Torres et al., 2010), and tentatively identified via mid-IR SEDs (Alonso-Herrero et al., 2013) and ionized Fe $K\alpha$ emission (Ballo et al., 2004). As reported by Ptak et al. (2015), Arp 299-B is detected by *NuSTAR* with a hard X-ray flux of $F_{10-30\text{ keV}} = 3.5 \times 10^{-12} \text{ erg cm}^{-2} \text{ s}^{-1}$, while Arp 299-A is dominated by X-ray binaries below 10 keV and contains no hard X-ray emitting AGN above a 10 – 30 keV limit of $< 3.5 \times 10^{-13} \text{ erg cm}^{-2} \text{ s}^{-1}$. Here we demonstrate that *HEX-P* would not only clearly detect both of the reported AGNs in Arp 299 in the 0.2-80 keV band but would spatially resolve the AGNs in both HET and LET imaging.

Our input models are informed by the model choices and spectral fitting results in Ptak et al. (2015). Specifically, we adopt the following model to describe the spectrum of each nucleus:

$$tbabs \times (borus + ztbabs \times cabs \times zcutoffpl + zcutoffpl) \quad (4)$$

where we have used the BORUS02 model (Baloković et al., 2018) rather than MYTorus, which was used by Ptak et al. (2015). This model incorporates host galaxy absorption (TBABS), reflected emission (BORUS02), an absorbed intrinsic power law that accounts for photoelectric absorption and Compton scattering, and a cut-off power law to account for soft X-ray emission from X-ray binaries. For Arp 299-B, we assume $\Gamma = 1.95$, $N_{\text{H}} = 4 \times 10^{24} \text{ cm}^{-2}$ (for simplicity we assume the average torus column density and the line-of-sight column density are equal), covering factor $\cos(\theta_{\text{open}}) = 0.85$, and we normalize the 10 – 30 keV emission to $3.5 \times 10^{-12} \text{ erg cm}^{-2} \text{ s}^{-1}$. For Arp 299-A, we assume $\Gamma = 1.8$, $N_{\text{H}} = 5 \times 10^{22} \text{ cm}^{-2}$ (since it is likely an unobscured, low luminosity AGN, e.g., Ptak et al., 2015), and covering factor $\cos(\theta_{\text{open}}) = 0.5$; while (Ptak et al., 2015) placed an upper limit of $< 3.5 \times 10^{-13} \text{ erg cm}^{-2} \text{ s}^{-1}$ on the 10 – 30 keV flux of Arp 299-A ($< 10\%$ of the observed flux of Arp 299-B), we conservatively assume that Arp 299-A (here, AGN 2) exhibits an observed 10 – 30 keV flux of $7 \times 10^{-14} \text{ erg cm}^{-2} \text{ s}^{-1}$ (i.e. 2% of the 10 – 30 keV observed flux of Arp 299-B). For both AGNs 1 and 2, we assume $\Gamma = 1.8$ and a cutoff energy of 7 keV for the power law component driven by X-ray binaries; for simplicity, we assume these components contribute equally to the total 2-10 keV XRB-driven flux ($8.1 \times 10^{-13} \text{ erg cm}^{-2} \text{ s}^{-1}$) found by Ptak et al. (2015), and we therefore normalize both components to $4.05 \times 10^{-13} \text{ erg cm}^{-2} \text{ s}^{-1}$ in the 2-10 keV band. For our spatial models, we adopt the positions given in Table 1 of Ptak et al. (2015). We once again simulated these AGNs using SOXS for SIMPUT file creation and SIXTE for event file and spectroscopic data product creation.

We show the simulated *HEX-P* LET and HET images in Figure 6 juxtaposed with the tricolor optical *ugz* imaging from the Dark Energy Camera Legacy Survey (DeCaLS) Legacy Viewer⁴ and simulated *NuSTAR*/FPMA imaging. At 21'' separation, the soft ($< 10 \text{ keV}$) X-ray components in the *NuSTAR* imaging were spatially blended, and above 10 keV the secondary nucleus is not detected by *NuSTAR* (see Figure 6 in Ptak et al., 2015). However, *HEX-P* clearly resolves the two nuclei in both the LET and HET imaging and detects the simulated low luminosity AGN in Arp 299-A at energies beyond 10 keV.

To demonstrate *HEX-P*'s spectroscopic capabilities, we fit LET and HET spectra extracted with 8'' and 18'' radius apertures, respectively. These aperture choices represent an enclosed energy fraction (EEF) of $\sim 100\%$ and naturally suffer from cross-contamination; in practice, aperture sizes that represent only 50%-60% EEF are more commonly used when extracting X-ray spectra and would suffer from less cross-contamination, but our aperture choices provide an additional test for *HEX-P*'s spectroscopic capabilities in

⁴ <https://www.legacysurvey.org/viewer>

discerning the properties of the distinct AGNs when spectral contamination is present. Arp 299 represents a prime example in which the LET spectra will be uncontaminated while each HET spectrum will contain contributions from both AGNs, which are separated by 21". Here we show how the LET can be used to improve the reliability of HET spectral fitting.

We perform the fitting of our simulated Arp 299 *HEX-P* spectra using v2.9 of the Bayesian X-ray Analysis (BXA; Buchner et al. 2014a; Buchner 2021a) software package, which connects PyXspec (Arnaud, 1996) to the nested sampling (Skilling, 2004; Buchner, 2023) algorithm MLFriends (Buchner et al., 2014b; Buchner, 2019) implemented in UltraNest (Buchner, 2021b). Our reasoning for using nested sampling here is two-fold. First, the global parameter exploration enables the traversal of high dimensionality parameter spaces in an efficient manner that is minimally affected by local minima. Second, the pre-defined convergence criteria for nested sampling ensures our fitting process is devoid of biases that can be imposed when fitting of simulated data is not performed in a blind manner (see e.g., Kammoun et al. 2022).

The resolving ability of the LET ensures negligible cross-contamination in the spectral extraction of both sources. However, despite the angular resolution of the HET being a considerable improvement on *NuSTAR* (see Figure 2), some cross-contamination remains (see also Figure 8). For this reason, we chose to fit the simulated LET and HET spectra for both AGN 1 and AGN 2 simultaneously whilst incorporating nuisance parameters to describe the amount of flux contamination in each source. Our spectral model thus includes the main spectral components used to simulate the AGNs, as well as a multiplicative factor to each AGN component to account for the relative contamination in each AGN HET \times 2 spectrum. We manually set the cross-contamination to zero for the LET spectra, since any contamination is negligible, and assume that each HET \times 2 spectrum contains 100% of the AGN emission that the extraction region was centered on and some fraction of the other AGN flux contaminating that extraction region.

We assigned log-uniform priors for all line-of-sight absorption, cross-contamination factors, high-energy cut-offs and normalizations. We additionally created custom cos-uniform priors for all variable obscurer geometric angles (namely the torus opening angle and line-of-sight inclination for both AGNs). Finally, the AGN photon indices were assigned Gaussian priors with mean 1.9 and 0.15 standard deviation and the X-ray binary photon index was assigned a uniform prior.

Figure 7 presents the fit acquired with BXA using a total of 18 free parameters. Owing to the combined broadband, sensitive coverage with the LET and HETs, we constrain the overall intrinsic X-ray luminosities and line-of-sight obscuration ($\log[N_{\text{H}}/\text{cm}^{-2}] = 24.60^{+0.04}_{-0.04}$ for Arp-299B and $\log[N_{\text{H}}/\text{cm}^{-2}] = 22.43^{+0.64}_{-0.29}$ for Arp-299A) for both AGN well. We additionally note that owing to the simultaneous broadband coverage of the LET and HETs, the spectral fit is additionally devoid of any variability concerns across the full ~ 0.2 –80 keV passband. By using BXA, we additionally recover the complex posterior degeneracies intricately associated with various system parameters, e.g., torus covering factors/opening angles ($\log[\theta_{\text{open}}] = 0.88^{+0.08}_{-0.13}$ for Arp-299B and $\log[\theta_{\text{open}}] = 0.54^{+0.30}_{-0.29}$ for Arp-299A), photon index ($\Gamma = 1.94^{+0.06}_{-0.10}$ for Arp-299B and $\Gamma = 1.89^{+0.14}_{-0.13}$ for Arp-299A), and intrinsic coronal normalisation, the latter two of which are important when propagating uncertainties into intrinsic luminosity estimates or Eddington ratios. These results clearly demonstrate our ability to reliably recover the intrinsic properties for each AGN despite the cross-contamination in the HET imaging.

6 SPECTROSCOPIC FITTING OF DUAL AGNS

Simultaneous fitting of soft (*Chandra* and/or *XMM-Newton*) and hard (*NuSTAR*) X-ray spectra has been successfully performed in the past for a few closely separated dual AGN (e.g., NGC 6240, Mrk 273,

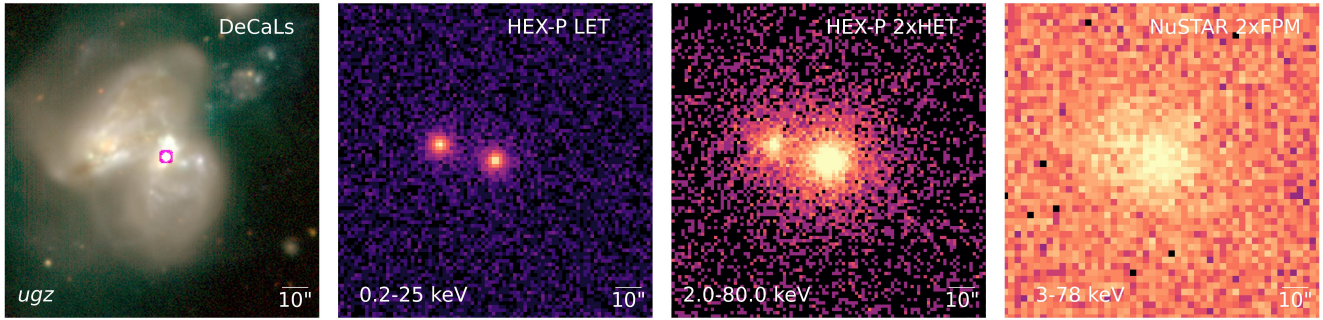


Figure 6. The Arp 299 case study: optical *ugz* imaging from DeCaLS (left panel), simulated 0.2-25 keV LET and 2-80 keV HET (2-camera) *HEX-P* imaging (middle panels), and observed 3-78 keV *NuSTAR* imaging of Arp 299. The energy band or filter is indicated in the bottom left corner of each panel, while the facility or image source resides in the top right corner of each panel. Scale bars in the bottom right corners indicate 10". The LET and HET images were simulated following the procedure in Section 5 and include spectral and spatial models for the X-ray binary populations and the two AGNs in the merger system. For simplicity, we assume the X-ray binary populations are limited to the nuclei and model them as point sources coincident with the nuclei rather than as extended sources. While the two AGNs cannot be clearly detected in the *NuSTAR* imaging (nor was Arp 299-A detected above 10 keV), the two AGNs can be clearly spatially resolved by both the LET and HET.

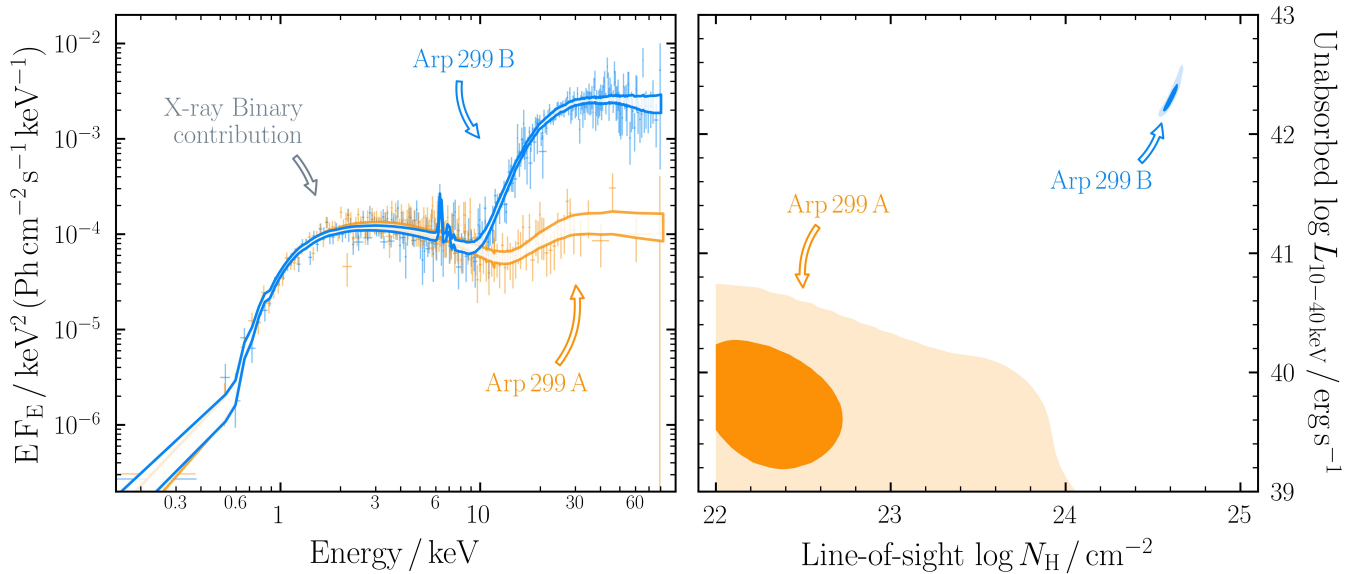


Figure 7. Simulated *HEX-P* HET (2-camera, co-added) and LET spectra, and the best-fitting models for the simulated Arp 299-A and Arp 299-B sources. The left panel shows the spectra unfolded with the best-fitting models while the right panel shows the contours for the best-fitting line-of-sight column densities and unabsorbed 10–40 keV luminosity in units of erg s^{-1} . Blue and orange data points and model curves correspond to the Arp 299-B and Arp 299-A, respectively. While we find a slightly harder power law slope for the X-ray binary power law component, we recover very similar values for the AGN power law slopes and column densities to those used in the input models.

Mrk 266 Nardini, 2017; Iwasawa et al., 2018, 2020). At these pair separations ($\sim 10''$ or lower), careful modeling using tools like BXA (Buchner et al., 2014b, see above) should be employed, as the spectra will be convolved at these pair separations and will contain contributions from both AGNs. We illustrate the level of flux contamination in Figure 8, which shows the estimated HET flux for each AGN as a function of pair separation, extracted from the co-added 2xHET images using 18" radius apertures ($\sim 100\%$ EEF;

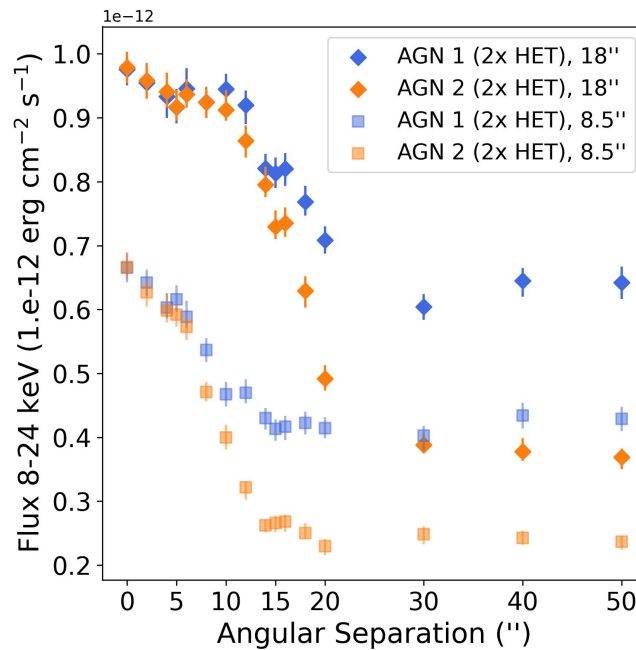


Figure 8. 8-24 keV observed fluxes from AGN 1 and 2 (from our general suite of simulations described in Sections 3 and 4.1) as a function of pair separation. Diamonds correspond to spectra extracted from 2-camera HET imaging using 18'' radius apertures ($\sim 100\%$ EEF), while squares correspond to spectra extracted from 2-camera HET imaging using 8.5'' radius apertures ($\sim 50\%$ EEF); these spectra were fit in XSPEC using the same input spectral model used to simulate the data, where only the normalizations were free to vary in order to recover the observed flux. While the sharp increase in spectral contamination (traced by the increasing flux of each AGN) at $\sim 18''$ for the larger apertures is due to our choice of aperture size, the sharp increase in contamination observed at $\sim 10''$ for the smaller apertures is more likely due to the size of the HET PSF itself.

diamonds) and 8.5'' apertures ($\sim 50\%$ EEF; squares) for each AGN. As the pair separation decreases, the two AGNs naturally contribute more to each other's observed flux as a result of the $\sim 17.5''$ HPD of the HET. The large jump in the observed fluxes at angular separations smaller than $\sim 18''$ extracted from the 18'' radius ($\sim 100\%$ EEF) apertures, particularly for the weaker AGN, is due to the aperture size rather than the HET PSF. When 8.5'' radius apertures are used ($\sim 50\%$ EEF), we find that spectral contamination appears to be modest at separations of $> 12''$ and becomes more significant at separations $< 12''$, despite our ability to visually resolve the two AGNs in the imaging. The LET, on the other hand, will offer relatively contamination-free spectra down to closer pair separations ($\lesssim 6''$). For this reason, it will become increasingly important at smaller pair separations to fit LET and HET AGN spectra simultaneously, because the LET spectra will bolster the accuracy of the X-ray spectral parameters derived from HET spectra.

7 SYNERGIES WITH UPCOMING FACILITIES

Given that dual AGNs are predicted to exhibit extremely red infrared colors (Blecha et al., 2018) in concert with high absorbing columns (e.g., Capelo et al., 2015; Blecha et al., 2018), infrared observations are a natural choice to pair with hard and soft X-ray imaging and spectroscopy from *HEX-P*. *Euclid*, the recently launched ESA near-IR and optical imaging and spectroscopy mission (Laureijs et al., 2011), will provide sub-arcsecond near-IR and optical imaging and near-IR spectroscopy across approximately one third of the sky by the time *HEX-P* launches. By the very nature of its mission design, *Euclid* will act

as a new dual AGN survey facility, forming an enormous archival sample of interacting and merging galaxies from which promising near-IR dual AGNs can be selected and followed-up with *HEX-P*. *JWST* will also offer unprecedented near- and mid-IR imaging and spectroscopic observations of small samples of dual AGNs (and candidates) found both within deep surveys (e.g., Comerford et al., 2009; Civano et al., 2010, 2012) and through targeted observations, and will provide the opportunity to probe not only heavily obscured AGNs but also heavily obscured star formation in, for example, dual AGNs hosted by LIRGs and ULIRGs (e.g., Komossa et al., 2003; Iwasawa et al., 2011; Torres-Albà et al., 2018). On the other hand, Extremely Large Telescopes (ELTs) – expected to come online in the 2030s – will usher in vast improvements in ground-based near-IR and optical spectroscopy and imaging and will experience substantially lower observational overheads and lower subscription rates than *JWST*. ELTs will therefore be paramount for targeting large samples of dual AGNs and may, like *Euclid*, represent the optimal dual AGN survey facilities that can work in tandem with *HEX-P*. In the meantime, high cadence, high resolution ($\lesssim 1''$ angular resolution) optical imaging with the upcoming Vera C. Rubin Observatory Ivezić et al. (2019) – in concert with presently available optical and near-IR data from *Euclid* – will also aid in the development and preliminary analyses of large samples of dual AGN candidates. The *Nancy Grace Roman Telescope*, slated for launch in the 2030s, will operate at infrared wavelengths with a FOV $100\times$ larger than *HST* with imaging sensitivity and PSF sizes superior to both *HST* and *Euclid*. *NGR*'s combination of FOV and wavelength coverage will make it an optimal facility for serendipitous dual AGN searches and studies and will complement both *Euclid* and *HEX-P*. Another important upcoming facility will be the ‘next-generation VLA’ (ngVLA, e.g., Burke-Spolaor et al., 2018), which will boast $10\times$ the sensitivity of the Jansky VLA and ALMA with $30\times$ longer baselines that will enable $0.01''$ – $0.001''$ resolution across the 1.2–116 GHz frequency range. Since radio is also immune to obscuration, the ngVLA will have the sensitivity and resolution to detect dual AGNs to $z \sim 1$, if they are sufficiently luminous in the radio. *HEX-P* and the ngVLA could work as separate follow-up facilities, or *HEX-P* could work in tandem with the ngVLA to confirm dual AGNs and measure the obscuring columns and try to constrain torus parameters (the latter of which the ngVLA would not be able to do). A joint *HEX-P*/ngVLA coverage strategy may be able to simultaneously circumvent X-ray and radio selection biases. In a similar vein, *HEX-P* observations in combination with ALMA 100–200 GHz continuum observations (Ricci et al., 2023) could offer unprecedented views to the most heavily obscured dual AGNs. Due to the reduced opacities in these ALMA bands, one can probe through very high column densities.

8 CONCLUSIONS

The *HEX-P* Probe-class mission concept combines high spatial resolution X-ray imaging ($\sim 17.5''$ HPD HET, $\sim 3.5''$ HPD LET) and broad spectral coverage (0.2–80 keV) with superior sensitivity to faint fluxes than current facilities and will usher in revolutionary new insights into dual AGN growth across the merger sequence. Hard X-ray imaging and spectroscopy is particularly important to the field of dual AGN science, as these systems are expected to be heavily obscured (e.g., Komossa et al., 2003; Bianchi et al., 2008; Mazzarella et al., 2012; Capelo et al., 2015; Blecha et al., 2018; Pfeifle et al., 2019b), making optical and soft X-ray missions biased against their detection and accurate analysis; *HEX-P* is the only Probe mission concept that can fulfil this scientific need. In this work, we have used a suite of dual AGN simulations - developed using SOXS (ZuHone et al., 2023) and SIXTE (Dauser et al., 2019) - to demonstrate the following:

- Without the aid of specialized detection algorithms, the spatial resolution of *HEX-P* LET and HET will allow us to resolve dual AGNs down to $\sim 3''$ and $\sim 5''$, respectively ($5''$ corresponds to ~ 4.9 kpc at

$z = 0.05$). NuSTAR, on the other hand, cannot spatially resolve dual AGNs below $\sim 18''$ (~ 17.9 kpc at $z = 0.05$).

- With the aid of Bayesian detection algorithms like that employed in this work, *HEX-P* will be able to confirm dual AGNs down to separations of $\sim 2''$ (~ 2.0 kpc at $z=0.05$) in both HET and LET imaging. The exact spatial resolution limit is determined by a combination of source flux levels and observation exposure time.
- Given *HEX-P*'s spatial resolution for both the LET and HET, *HEX-P* will have the capability to probe dual AGNs in late-stage mergers (< 10 kpc) out to $z \sim 0.1$, and intermediate-stage mergers (~ 30 kpc) out to redshifts of $z \sim 0.3$. This is a dramatic improvement over *NuSTAR*, which cannot probe dual AGNs with even 50 kpc separations beyond $z \sim 0.25$.
- *HEX-P* will enable distinct (relatively contamination free) spectral analyses with the LET in the 0.2-25 keV band down to separations of $\sim 6 - 8''$, while the HET will offer relatively contamination free spectral analyses down to separations of $\sim 10''$ (assuming apertures encompassing $\sim 50\%$ EEf are employed). At small angular separations, this contamination can be mitigated by fitting LET and HET spectra simultaneously, and including model component constants that account for spectral contamination.

HEX-P is poised to transform the landscape of dual AGN science, offering one of the cleanest methods of AGN detection that will be largely obscuration independent given the hard X-ray bandpass and enhanced faint source sensitivity of the HET. *HEX-P* will play a key role in uncovering heretofore unconfirmed dual AGNs in candidate systems, determining the occupation fraction of hard X-ray emitting and obscured dual AGNs in known and currently unknown dual AGN populations, and studying the fueling and obscuration levels of dual AGNs across the merger sequence and as a function of AGN type in the local Universe. Such observations will refine previously proposed correlations between the projected pair separations of the AGNs and their X-ray luminosities (Koss et al., 2012; Hou et al., 2020) and column densities (Guainazzi et al., 2021). Bayesian detection algorithms akin to BAYMAX (Foord et al., 2019, 2020, 2021) will provide statistically powerful improvements to the detectability of closely-separated sources, and such Bayesian methods will provide more accurate constraints on the flux ratios of close angular pairs and thereby improve the statistical priors used during the spectral fitting process. Furthermore, with the high sensitivity and angular resolution of the LET, *HEX-P* will allow the simultaneous examination of the host stellar populations via the detection of hot star formation-driven components in the soft X-rays, often observed in dual AGNs (see Section 5.4 in Pfeifle et al., 2023). Thus, *HEX-P* will also probe connections between dual AGN activation and obscuration with the properties of the host stellar populations.

CONFLICT OF INTEREST STATEMENT

The authors declare that the research was conducted in the absence of any commercial or financial relationships that could be construed as a potential conflict of interest. R. W. P. is a member of the *HEX-P* AGN Science Working Group and is also currently a co-deputy for the Line Emission Mapper (LEM) AGN Working Group; both of these are current mission concept studies.

AUTHOR CONTRIBUTIONS

R. W. P. led the work, developed the SOXS, SIXTE, and Jupyter Notebook scripts used to generate all of the simulated event files, science images, and spectroscopic data products for this study; he led all analysis of spatial resolution and spectral signal-to-noise. P. G. B. assisted with the generation of spectroscopic data

products and performed the spectroscopic data analysis for the Arp 299 test case in this work. K. A. W. provided guidance for the scientific content of this work. J. B. developed the UltraNest-based Bayesian source detection algorithm used for the spatial resolution source detection analysis in this work. F. C. and P. G. B., as science lead and deputy lead for the *HEX-P* AGN working group, provided general guidance for the science content of this work. All authors reviewed the manuscript and provided feedback to improve the state of the manuscript.

FUNDING

R.W.P. gratefully acknowledges support through an appointment to the NASA Postdoctoral Program at Goddard Space Flight Center, administered by ORAU through a contract with NASA. The work of D.S. was carried out at the Jet Propulsion Laboratory, California Institute of Technology, under a contract with NASA. C.R. acknowledges support from Fondecyt Regular grant 1230345 and ANID BASAL project FB210003. E.K. acknowledges financial support from the Centre National d'Etudes Spatiales (CNES). L.M. is supported by the CITA National Fellowship.

ACKNOWLEDGMENTS

We thank the SIXTE support team (with particular thanks to Ole König) for their assistance in generating spectra from simulated event files and for assistance with the documentation.

DATA AVAILABILITY STATEMENT

The SIXTE and SOXS scripts along with the Jupyter Notebooks used to generate and analyze the simulated data sets for this study can be found in the following GitHub repository⁵ owned by R. W. P. Note, the actual data products are not included in this remote repository due to the size of the files, but the scripts and Notebooks can be used to regenerate all of the data products created for this work. Copies of the simulated data are available upon request.

9 APPENDIX

REFERENCES

- Akaike, H. (1974). A New Look at the Statistical Model Identification. *IEEE Transactions on Automatic Control* 19, 716–723
- Alonso-Herrero, A., Roche, P. F., Esquej, P., González-Martín, O., Pereira-Santaella, M., Ramos Almeida, C., et al. (2013). Uncovering the Deeply Embedded Active Galactic Nucleus Activity in the Nuclear Regions of the Interacting Galaxy Arp 299. *ApJL* 779, L14. doi:10.1088/2041-8205/779/1/L14
- Amaro-Seoane, P., Andrews, J., Arca Sedda, M., Askar, A., Baghi, Q., Balasov, R., et al. (2023). Astrophysics with the Laser Interferometer Space Antenna. *Living Reviews in Relativity* 26, 2. doi:10.1007/s41114-022-00041-y
- Arnaud, K. A. (1996). XSPEC: The First Ten Years. In *Astronomical Data Analysis Software and Systems V*, eds. G. H. Jacoby and J. Barnes. vol. 101 of *Astronomical Society of the Pacific Conference Series*, 17
- Ballo, L., Braitto, V., Della Ceca, R., Maraschi, L., Tavecchio, F., and Dadina, M. (2004). Arp 299: A Second Merging System with Two Active Nuclei? *ApJ* 600, 634–639. doi:10.1086/379887

⁵ <https://github.com/thatastroguy/HEXP>

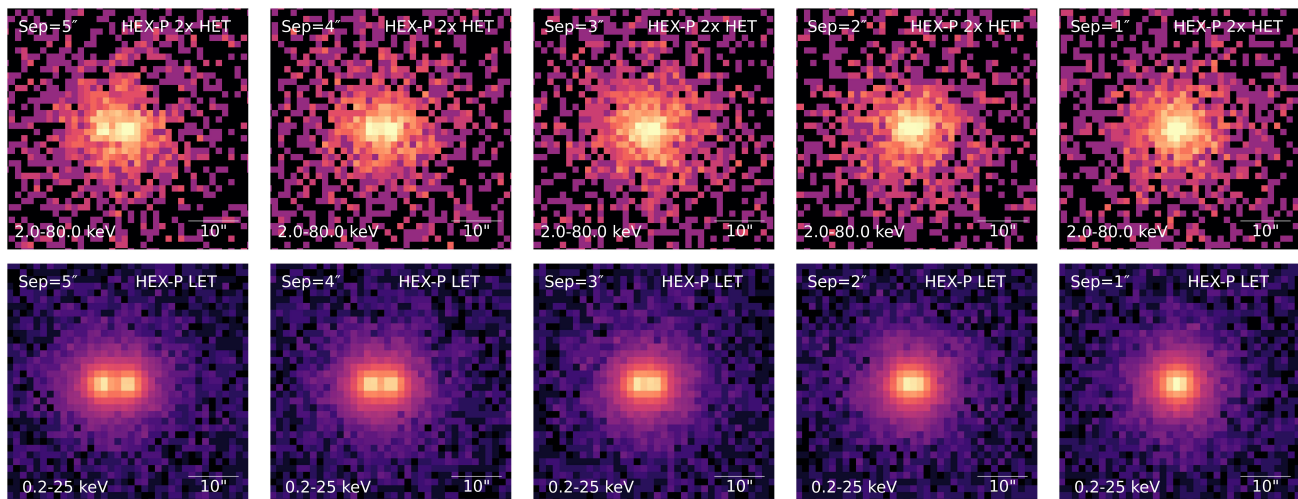


Figure 9. This 8-panel figure highlights the *HEX-P* HET and LET imaging for pair separations ranging from 5'' down to 1''. With the exception of the choice of pair separations, these panels are identical in design as Figure 1 and 2. Here we can identify pairs of sources down to $\sim 4''$ in the HET and $\sim 3''$ in the LET by eye. See Section 4.1 on algorithmically detecting even more closely separated sources in *HEX-P* imaging.

- Baloković, M., Brightman, M., Harrison, F. A., Comastri, A., Ricci, C., Buchner, J., et al. (2018). New Spectral Model for Constraining Torus Covering Factors from Broadband X-Ray Spectra of Active Galactic Nuclei. *ApJ* 854, 42. doi:10.3847/1538-4357/aaa7eb
- Barnes, J. E. and Hernquist, L. (1996). Transformations of Galaxies. II. Gasdynamics in Merging Disk Galaxies. *ApJ* 471, 115. doi:10.1086/177957
- Barnes, J. E. and Hernquist, L. E. (1991). Fueling Starburst Galaxies with Gas-rich Mergers. *ApJL* 370, L65. doi:10.1086/185978
- Barrows, R. S., Comerford, J. M., Stern, D., and Assef, R. J. (2023). A Census of WISE-selected Dual and Offset AGNs Across the Sky: New Constraints on Merger-driven Triggering of Obscured AGNs. *ApJ* 951, 92. doi:10.3847/1538-4357/acd2d3
- Bianchi, S., Chiaberge, M., Piconcelli, E., Guainazzi, M., and Matt, G. (2008). Chandra unveils a binary active galactic nucleus in Mrk 463. *MNRAS* 386, 105–110. doi:10.1111/j.1365-2966.2008.13078.x
- Blecha, L., Snyder, G. F., Satyapal, S., and Ellison, S. L. (2018). The power of infrared AGN selection in mergers: a theoretical study. *MNRAS* 478, 3056–3071. doi:10.1093/mnras/sty1274
- Buchner, J. (2019). Collaborative Nested Sampling: Big Data versus Complex Physical Models. *PASP* 131, 108005. doi:10.1088/1538-3873/aae7fc
- Buchner, J. (2021a). Bayesian X-ray Analysis (BXA) v4.0. *The Journal of Open Source Software* 6, 3045. doi:10.21105/joss.03045
- Buchner, J. (2021b). UltraNest - a robust, general purpose Bayesian inference engine. *The Journal of Open Source Software* 6, 3001. doi:10.21105/joss.03001
- Buchner, J. (2023). Nested sampling methods. *Statistics Surveys* 17, arXiv:2101.09675. doi:10.1214/23-SS144
- Buchner, J., Georgakakis, A., Nandra, K., Hsu, L., Rangel, C., Brightman, M., et al. (2014a). X-ray spectral modelling of the AGN obscuring region in the CDFS: Bayesian model selection and catalogue. *A&A* 564, A125. doi:10.1051/0004-6361/201322971

- Buchner, J., Georgakakis, A., Nandra, K., Hsu, L., Rangel, C., Brightman, M., et al. (2014b). X-ray spectral modelling of the AGN obscuring region in the CDFS: Bayesian model selection and catalogue. *A&A* 564, A125. doi:10.1051/0004-6361/201322971
- Burke-Spolaor, S., Blecha, L., Bogdanovic, T., Comerford, J. M., Lazio, T. J. W., Liu, X., et al. (2018). The Next-Generation Very Large Array: Supermassive Black Hole Pairs and Binaries. *arXiv e-prints*, arXiv:1808.04368doi:10.48550/arXiv.1808.04368
- Callegari, S., Kazantzidis, S., Mayer, L., Colpi, M., Bellovary, J. M., Quinn, T., et al. (2011). Growing Massive Black Hole Pairs in Minor Mergers of Disk Galaxies. *ApJ* 729, 85. doi:10.1088/0004-637X/729/2/85
- Callegari, S., Mayer, L., Kazantzidis, S., Colpi, M., Governato, F., Quinn, T., et al. (2009). Pairing of Supermassive Black Holes in Unequal-Mass Galaxy Mergers. *ApJL* 696, L89–L92. doi:10.1088/0004-637X/696/1/L89
- Capelo, P. R., Dotti, M., Volonteri, M., Mayer, L., Bellovary, J. M., and Shen, S. (2017). A survey of dual active galactic nuclei in simulations of galaxy mergers: frequency and properties. *MNRAS* 469, 4437–4454. doi:10.1093/mnras/stx1067
- Capelo, P. R., Volonteri, M., Dotti, M., Bellovary, J. M., Mayer, L., and Governato, F. (2015). Growth and activity of black holes in galaxy mergers with varying mass ratios. *MNRAS* 447, 2123–2143. doi:10.1093/mnras/stu2500
- Ciurlo, A., Mannucci, F., Yeh, S., Amiri, A., Carniani, S., Cicone, C., et al. (2023). New multiple AGN systems with subarcsec separation: Confirmation of candidates selected via the novel GMP method. *A&A* 671, L4. doi:10.1051/0004-6361/202345853
- Civano, F., Elvis, M., Lanzuisi, G., Aldcroft, T., Trichas, M., Bongiorno, A., et al. (2012). Chandra High-resolution observations of CID-42, a Candidate Recoiling Supermassive Black Hole. *ApJ* 752, 49. doi:10.1088/0004-637X/752/1/49
- Civano, F., Elvis, M., Lanzuisi, G., Jahnke, K., Zamorani, G., Blecha, L., et al. (2010). A Runaway Black Hole in COSMOS: Gravitational Wave or Slingshot Recoil? *ApJ* 717, 209–222. doi:10.1088/0004-637X/717/1/209
- Civano, F., Hickox, R. C., Puccetti, S., Comastri, A., Mullaney, J. R., Zappacosta, L., et al. (2015). The Nustar Extragalactic Surveys: Overview and Catalog from the COSMOS Field. *ApJ* 808, 185. doi:10.1088/0004-637X/808/2/185
- Comerford, J. M., Gerke, B. F., Stern, D., Cooper, M. C., Weiner, B. J., Newman, J. A., et al. (2012). Kiloparsec-scale Spatial Offsets in Double-peaked Narrow-line Active Galactic Nuclei. I. Markers for Selection of Compelling Dual Active Galactic Nucleus Candidates. *ApJ* 753, 42. doi:10.1088/0004-637X/753/1/42
- Comerford, J. M., Griffith, R. L., Gerke, B. F., Cooper, M. C., Newman, J. A., Davis, M., et al. (2009). 1.75 h⁻¹ kpc Separation Dual Active Galactic Nuclei at z = 0.36 in the Cosmos Field. *ApJL* 702, L82–L86. doi:10.1088/0004-637X/702/1/L82
- Comerford, J. M., Pooley, D., Barrows, R. S., Greene, J. E., Zakamska, N. L., Madejski, G. M., et al. (2015). Merger-driven Fueling of Active Galactic Nuclei: Six Dual and Offset AGNs Discovered with Chandra and Hubble Space Telescope Observations. *ApJ* 806, 219. doi:10.1088/0004-637X/806/2/219
- Comerford, J. M., Pooley, D., Gerke, B. F., and Madejski, G. M. (2011). Chandra Observations of a 1.9 kpc Separation Double X-Ray Source in a Candidate Dual Active Galactic Nucleus Galaxy at z = 0.16. *ApJL* 737, L19. doi:10.1088/2041-8205/737/1/L19
- Dauser, T., Falkner, S., Lorenz, M., Kirsch, C., Peille, P., Cucchetti, E., et al. (2019). SIXTE: a generic X-ray instrument simulation toolkit. *A&A* 630, A66. doi:10.1051/0004-6361/201935978

- De Rosa, A., Vignali, C., Husemann, B., Bianchi, S., Bogdanović, T., Guainazzi, M., et al. (2018). Disclosing the properties of low-redshift dual AGN through XMM-Newton and SDSS spectroscopy. *MNRAS* 480, 1639–1655. doi:10.1093/mnras/sty1867
- De Rosa, A., Vignali, C., Severgnini, P., Bianchi, S., Bogdanović, T., Charisi, M., et al. (2023). The X-ray view of optically selected dual AGN. *MNRAS* 519, 5149–5160. doi:10.1093/mnras/stac3664
- Ellison, S. L., Patton, D. R., Mendel, J. T., and Scudder, J. M. (2011). Galaxy pairs in the Sloan Digital Sky Survey - IV. Interactions trigger active galactic nuclei. *MNRAS* 418, 2043–2053. doi:10.1111/j.1365-2966.2011.19624.x
- Ellison, S. L., Secrest, N. J., Mendel, J. T., Satyapal, S., and Simard, L. (2017). Discovery of a dual active galactic nucleus with ~ 8 kpc separation. *MNRAS* 470, L49–L53. doi:10.1093/mnrasl/slx076
- Eraerds, T., Antonelli, V., Davis, C., Hall, D., Hetherington, O., Holland, A., et al. (2021). Enhanced simulations on the Athena/Wide Field Imager instrumental background. *Journal of Astronomical Telescopes, Instruments, and Systems* 7, 034001. doi:10.1117/1.JATIS.7.3.034001
- Foord, A., Gültekin, K., Nevin, R., Comerford, J. M., Hodges-Kluck, E., Barrows, R. S., et al. (2020). A Second Look at 12 Candidate Dual AGNs Using BAYMAX. *ApJ* 892, 29. doi:10.3847/1538-4357/ab72fa
- Foord, A., Gültekin, K., Reynolds, M. T., Hodges-Kluck, E., Cackett, E. M., Comerford, J. M., et al. (2019). A Bayesian Analysis of SDSS J0914+0853, a Low-mass Dual AGN Candidate. *ApJ* 877, 17. doi:10.3847/1538-4357/ab18a3
- Foord, A., Gültekin, K., Runnoe, J. C., and Koss, M. J. (2021). AGN Triality of Triple Mergers: Detection of Faint X-Ray Point Sources. *ApJ* 907, 71. doi:10.3847/1538-4357/abce5d
- Frey, S., Paragi, Z., An, T., and Gabányi, K. É. (2012). Two in one? A possible dual radio-emitting nucleus in the quasar SDSS J1425+3231. *MNRAS* 425, 1185–1191. doi:10.1111/j.1365-2966.2012.21491.x
- Fu, H., Myers, A. D., Djorgovski, S. G., Yan, L., Wrobel, J. M., and Stockton, A. (2015a). Radio-selected Binary Active Galactic Nuclei from the Very Large Array Stripe 82 Survey. *ApJ* 799, 72. doi:10.1088/0004-637X/799/1/72
- Fu, H., Wrobel, J. M., Myers, A. D., Djorgovski, S. G., and Yan, L. (2015b). Binary Active Galactic Nuclei in Stripe 82: Constraints on Synchronized Black Hole Accretion in Major Mergers. *ApJL* 815, L6. doi:10.1088/2041-8205/815/1/L6
- Fu, H., Zhang, Z.-Y., Assef, R. J., Stockton, A., Myers, A. D., Yan, L., et al. (2011). A Kiloparsec-scale Binary Active Galactic Nucleus Confirmed by the Expanded Very Large Array. *ApJL* 740, L44. doi:10.1088/2041-8205/740/2/L44
- Gabányi, K. É., An, T., Frey, S., Komossa, S., Paragi, Z., Hong, X. Y., et al. (2016). Four Dual AGN Candidates Observed with the VLBA. *ApJ* 826, 106. doi:10.3847/0004-637X/826/2/106
- Gabányi, K. É., Frey, S., Xiao, T., Paragi, Z., An, T., Kun, E., et al. (2014). A single radio-emitting nucleus in the dual AGN candidate NGC 5515. *MNRAS* 443, 1509–1514. doi:10.1093/mnras/stu1234
- Ge, J.-Q., Hu, C., Wang, J.-M., Bai, J.-M., and Zhang, S. (2012). Double-peaked Narrow Emission-line Galaxies from the Sloan Digital Sky Survey. I. Sample and Basic Properties. *ApJS* 201, 31. doi:10.1088/0067-0049/201/2/31
- Goulding, A. D., Pardo, K., Greene, J. E., Mingarelli, C. M. F., Nyland, K., and Strauss, M. A. (2019). Discovery of a Close-separation Binary Quasar at the Heart of a $z \sim 0.2$ Merging Galaxy and Its Implications for Low-frequency Gravitational Waves. *ApJL* 879, L21. doi:10.3847/2041-8213/ab2a14
- Gross, A. C., Fu, H., Myers, A. D., Wrobel, J. M., and Djorgovski, S. G. (2019). X-Ray Properties of Radio-selected Dual Active Galactic Nuclei. *ApJ* 883, 50. doi:10.3847/1538-4357/ab3795

- Guainazzi, M., De Rosa, A., Bianchi, S., Husemann, B., Bogdanovic, T., Komossa, S., et al. (2021). An XMM-Newton study of active-inactive galaxy pairs. *MNRAS* 504, 393–405. doi:10.1093/mnras/stab808
- Guainazzi, M., Piconcelli, E., Jiménez-Bailón, E., and Matt, G. (2005). The early stage of a cosmic collision? XMM-Newton unveils two obscured AGN in the galaxy pair ESO509-IG066. *A&A* 429, L9–L12. doi:10.1051/0004-6361:200400104
- Harrison, F. A., Craig, W. W., Christensen, F. E., Hailey, C. J., Zhang, W. W., Boggs, S. E., et al. (2013). The Nuclear Spectroscopic Telescope Array (NuSTAR) High-energy X-Ray Mission. *ApJ* 770, 103. doi:10.1088/0004-637X/770/2/103
- Hopkins, P. F., Hernquist, L., Cox, T. J., Di Matteo, T., Robertson, B., and Springel, V. (2006). A Unified, Merger-driven Model of the Origin of Starbursts, Quasars, the Cosmic X-Ray Background, Supermassive Black Holes, and Galaxy Spheroids. *ApJS* 163, 1–49. doi:10.1086/499298
- Hopkins, P. F., Hernquist, L., Cox, T. J., and Kereš, D. (2008). A Cosmological Framework for the Co-Evolution of Quasars, Supermassive Black Holes, and Elliptical Galaxies. I. Galaxy Mergers and Quasar Activity. *ApJS* 175, 356–389. doi:10.1086/524362
- Hou, M., Li, Z., and Liu, X. (2020). A Chandra X-Ray Survey of Optically Selected AGN Pairs. *ApJ* 900, 79. doi:10.3847/1538-4357/aba4a7
- Hou, M., Li, Z., Liu, X., Li, Z., Li, R., Wang, R., et al. (2023). NOEMA Detection of Circumnuclear Molecular Gas in X-Ray Weak Dual Active Galactic Nuclei: No Evidence for Heavy Obscuration. *ApJ* 943, 50. doi:10.3847/1538-4357/acaaf9
- Hou, M., Liu, X., Guo, H., Li, Z., Shen, Y., and Green, P. J. (2019). Active Galactic Nucleus Pairs from the Sloan Digital Sky Survey. III. Chandra X-Ray Observations Unveil Obscured Double Nuclei. *ApJ* 882, 41. doi:10.3847/1538-4357/ab3225
- Hwang, H.-C., Hamer, J. H., Zakamska, N. L., and Schlafman, K. C. (2020). Very wide companion fraction from Gaia DR2: A weak or no enhancement for hot Jupiter hosts, and a strong enhancement for contact binaries. *MNRAS* 497, 2250–2259. doi:10.1093/mnras/staa2124
- Imanishi, M., Kawamuro, T., Kikuta, S., Nakano, S., and Saito, Y. (2020). Subaru Infrared Adaptive Optics-assisted High-spatial-resolution Imaging Search for Luminous Dual Active Galactic Nuclei in Nearby Ultraluminous Infrared Galaxies. *ApJ* 891, 140. doi:10.3847/1538-4357/ab733e
- Imanishi, M. and Saito, Y. (2014). Subaru Adaptive-optics High-spatial-resolution Infrared K- and L'-band Imaging Search for Deeply Buried Dual AGNs in Merging Galaxies. *ApJ* 780, 106. doi:10.1088/0004-637X/780/1/106
- Ivezić, Ž., Kahn, S. M., Tyson, J. A., Abel, B., Acosta, E., Allsman, R., et al. (2019). LSST: From Science Drivers to Reference Design and Anticipated Data Products. *ApJ* 873, 111. doi:10.3847/1538-4357/ab042c
- Iwasawa, K., Ricci, C., Privon, G. C., Torres-Albà, N., Inami, H., Charmandaris, V., et al. (2020). A Compton-thick nucleus in the dual active galactic nuclei of Mrk 266. *A&A* 640, A95. doi:10.1051/0004-6361/202038513
- Iwasawa, K., Sanders, D. B., Teng, S. H., U, V., Armus, L., Evans, A. S., et al. (2011). C-GOALS: Chandra observations of a complete sample of luminous infrared galaxies from the IRAS Revised Bright Galaxy Survey. *A&A* 529, A106. doi:10.1051/0004-6361/201015264
- Iwasawa, K., U, V., Mazzarella, J. M., Medling, A. M., Sanders, D. B., and Evans, A. S. (2018). Testing a double AGN hypothesis for Mrk 273. *A&A* 611, A71. doi:10.1051/0004-6361/201731662
- Jansen, F., Lumb, D., Altieri, B., Clavel, J., Ehle, M., Erd, C., et al. (2001). XMM-Newton observatory. I. The spacecraft and operations. *A&A* 365, L1–L6. doi:10.1051/0004-6361:20000036

- Kammoun, E. S., Barret, D., Peille, P., Willingale, R., Dauser, T., Wilms, J., et al. (2022). The defocused observations of bright sources with Athena/X-IFU. *A&A* 664, A29. doi:10.1051/0004-6361/202243606
- Komossa, S., Burwitz, V., Hasinger, G., Predehl, P., Kaastra, J. S., and Ikebe, Y. (2003). Discovery of a Binary Active Galactic Nucleus in the Ultraluminous Infrared Galaxy NGC 6240 Using Chandra. *ApJL* 582, L15–L19. doi:10.1086/346145
- Kosec, P., Brightman, M., Stern, D., Müller-Sánchez, F., Koss, M., Oh, K., et al. (2017). Investigating the Evolution of the Dual AGN System ESO 509-IG066. *ApJ* 850, 168. doi:10.3847/1538-4357/aa932e
- Koss, M., Mushotzky, R., Treister, E., Veilleux, S., Vasudevan, R., and Trippe, M. (2012). Understanding Dual Active Galactic Nucleus Activation in the nearby Universe. *ApJL* 746, L22. doi:10.1088/2041-8205/746/2/L22
- Koss, M. J., Glidden, A., Baloković, M., Stern, D., Lamperti, I., Assef, R., et al. (2016). NuSTAR Resolves the First Dual AGN above 10 keV in SWIFT J2028.5+2543. *ApJL* 824, L4. doi:10.3847/2041-8205/824/1/L4
- Koss, M. J., Treister, E., Kakkad, D., Casey-Clyde, J. A., Kawamuro, T., Williams, J., et al. (2023). UGC 4211: A Confirmed Dual Active Galactic Nucleus in the Local Universe at 230 pc Nuclear Separation. *ApJL* 942, L24. doi:10.3847/2041-8213/aca8f0
- LaMassa, S. M., Yaqoob, T., Boorman, P. G., Tzanavaris, P., Levenson, N. A., Gandhi, P., et al. (2019). NuSTAR Uncovers an Extremely Local Compton-thick AGN in NGC 4968. *ApJ* 887, 173. doi:10.3847/1538-4357/ab552c
- LaMassa, S. M., Yaqoob, T., Levenson, N. A., Boorman, P., Heckman, T. M., Gandhi, P., et al. (2017). Chandra Reveals Heavy Obscuration and Circumnuclear Star Formation in Seyfert 2 Galaxy NGC 4968. *ApJ* 835, 91. doi:10.3847/1538-4357/835/1/91
- Laureijs, R., Amiaux, J., Arduini, S., Auguères, J. L., Brinchmann, J., Cole, R., et al. (2011). Euclid Definition Study Report. *arXiv e-prints*, arXiv:1110.3193doi:10.48550/arXiv.1110.3193
- Li, K., Ballantyne, D. R., and Bogdanović, T. (2021). The Detectability of Kiloparsec-scale Dual Active Galactic Nuclei: The Impact of Galactic Structure and Black Hole Orbital Properties. *ApJ* 916, 110. doi:10.3847/1538-4357/ac06a0
- Liu, X., Civano, F., Shen, Y., Green, P., Greene, J. E., and Strauss, M. A. (2013). Chandra X-Ray and Hubble Space Telescope Imaging of Optically Selected Kiloparsec-scale Binary Active Galactic Nuclei. I. Nature of the Nuclear Ionizing Sources. *ApJ* 762, 110. doi:10.1088/0004-637X/762/2/110
- Liu, X., Shen, Y., Strauss, M. A., and Greene, J. E. (2010). Type 2 Active Galactic Nuclei with Double-Peaked [O III] Lines: Narrow-Line Region Kinematics or Merging Supermassive Black Hole Pairs? *ApJ* 708, 427–434. doi:10.1088/0004-637X/708/1/427
- Liu, X., Shen, Y., Strauss, M. A., and Hao, L. (2011). Active Galactic Nucleus Pairs from the Sloan Digital Sky Survey. I. The Frequency on ~5-100 kpc Scales. *ApJ* 737, 101. doi:10.1088/0004-637X/737/2/101
- Mannucci, F., Pancino, E., Belfiore, F., Ciccone, C., Ciurlo, A., Cresci, G., et al. (2022). Unveiling the population of dual and lensed active galactic nuclei at sub-arcsec separations. *Nature Astronomy* 6, 1185–1192. doi:10.1038/s41550-022-01761-5
- Marchesi, S., Ajello, M., Marcotulli, L., Comastri, A., Lanzuisi, G., and Vignali, C. (2018). Compton-thick AGNs in the NuSTAR Era. *ApJ* 854, 49. doi:10.3847/1538-4357/aaa410
- Marchesi, S., Ajello, M., Zhao, X., Comastri, A., La Parola, V., and Segreto, A. (2019). Compton-thick AGNs in the NuSTAR Era. V. Joint NuSTAR and XMM-Newton Spectral Analysis of Three “Soft-gamma” Candidate CT-AGNs in the Swift/BAT 100-month Catalog. *ApJ* 882, 162. doi:10.3847/1538-4357/ab340a

- Mazzarella, J. M., Iwasawa, K., Vavilkin, T., Armus, L., Kim, D. C., Bothun, G., et al. (2012). Investigation of Dual Active Nuclei, Outflows, Shock-heated Gas, and Young Star Clusters in Markarian 266. *AJ* 144, 125. doi:10.1088/0004-6256/144/5/125
- Meidinger, N., Albrecht, S., Beitler, C., Bonholzer, M., Emberger, V., Frank, J., et al. (2020). Development status of the wide field imager instrument for Athena. In *Society of Photo-Optical Instrumentation Engineers (SPIE) Conference Series*. vol. 11444 of *Society of Photo-Optical Instrumentation Engineers (SPIE) Conference Series*, 114440T. doi:10.1117/12.2560507
- Müller-Sánchez, F., Comerford, J. M., Nevin, R., Barrows, R. S., Cooper, M. C., and Greene, J. E. (2015). The Origin of Double-peaked Narrow Lines in Active Galactic Nuclei. I. Very Large Array Detections of Dual AGNs and AGN Outflows. *ApJ* 813, 103. doi:10.1088/0004-637X/813/2/103
- Müller-Sánchez, F., Nevin, R., Comerford, J. M., Davies, R. I., Privon, G. C., and Treister, E. (2018). Two separate outflows in the dual supermassive black hole system NGC 6240. *Nature* 556, 345–348. doi:10.1038/s41586-018-0033-2
- Nandra, K., Barret, D., Barcons, X., Fabian, A., den Herder, J.-W., Piro, L., et al. (2013). The Hot and Energetic Universe: A White Paper presenting the science theme motivating the Athena+ mission. *arXiv e-prints*, arXiv:1306.2307doi:10.48550/arXiv.1306.2307
- Nardini, E. (2017). Nuclear absorption and emission in the AGN merger NGC 6240 : the hard X-ray view. *MNRAS* 471, 3483–3493. doi:10.1093/mnras/stx1878
- Oda, S., Ueda, Y., Tanimoto, A., and Ricci, C. (2018). Hard X-Ray View of HCG 16 (Arp 318). *ApJ* 855, 79. doi:10.3847/1538-4357/aaaccc
- Pérez-Torres, M. A., Alberdi, A., Romero-Cañizales, C., and Bondi, M. (2010). Serendipitous discovery of the long-sought active galactic nucleus in Arp 299-A. *A&A* 519, L5. doi:10.1051/0004-6361/201015462
- Pfeifle, R. W., Satyapal, S., Manzano-King, C., Cann, J., Sexton, R. O., Rothberg, B., et al. (2019a). A Triple AGN in a Mid-infrared Selected Late-stage Galaxy Merger. *ApJ* 883, 167. doi:10.3847/1538-4357/ab3a9b
- Pfeifle, R. W., Satyapal, S., Secrest, N. J., Gliozzi, M., Ricci, C., Ellison, S. L., et al. (2019b). Buried Black Hole Growth in IR-selected Mergers: New Results from Chandra. *ApJ* 875, 117. doi:10.3847/1538-4357/ab07bc
- Pfeifle, R. W., Weaver, K., Satyapal, S., Ricci, C., Secrest, N. J., Gliozzi, M., et al. (2023). NuSTAR Observations of Four Mid-IR Selected Dual AGN Candidates in Galaxy Mergers. *arXiv e-prints*, arXiv:2306.16437doi:10.48550/arXiv.2306.16437
- Piconcelli, E., Vignali, C., Bianchi, S., Mathur, S., Fiore, F., Guainazzi, M., et al. (2010). Witnessing the Key Early Phase of Quasar Evolution: An Obscured Active Galactic Nucleus Pair in the Interacting Galaxy IRAS 20210+1121. *ApJL* 722, L147–L151. doi:10.1088/2041-8205/722/2/L147
- Ptak, A., Hornschemeier, A., Zezas, A., Lehmer, B., Yukita, M., Wik, D., et al. (2015). A Focused, Hard X-Ray Look at Arp 299 with NuSTAR. *ApJ* 800, 104. doi:10.1088/0004-637X/800/2/104
- Ricci, C., Bauer, F. E., Treister, E., Schawinski, K., Privon, G. C., Blecha, L., et al. (2017). Growing supermassive black holes in the late stages of galaxy mergers are heavily obscured. *MNRAS* 468, 1273–1299. doi:10.1093/mnras/stx173
- Ricci, C., Chang, C.-S., Kawamuro, T., Privon, G. C., Mushotzky, R., Trakhtenbrot, B., et al. (2023). A Tight Correlation between Millimeter and X-Ray Emission in Accreting Massive Black Holes from ~ 100 mas Resolution ALMA Observations. *ApJL* 952, L28. doi:10.3847/2041-8213/acda27
- Ricci, C., Privon, G. C., Pfeifle, R. W., Armus, L., Iwasawa, K., Torres-Albà, N., et al. (2021). A hard X-ray view of luminous and ultra-luminous infrared galaxies in GOALS - I. AGN obscuration along the merger sequence. *MNRAS* 506, 5935–5950. doi:10.1093/mnras/stab2052

- Rubinur, K., Das, M., and Kharb, P. (2019). Searching for dual AGN in galaxies with double-peaked emission line spectra using radio observations. *MNRAS* 484, 4933–4950. doi:10.1093/mnras/stz334
- Satyapal, S., Ellison, S. L., McAlpine, W., Hickox, R. C., Patton, D. R., and Mendel, J. T. (2014). Galaxy pairs in the Sloan Digital Sky Survey - IX. Merger-induced AGN activity as traced by the Wide-field Infrared Survey Explorer. *MNRAS* 441, 1297–1304. doi:10.1093/mnras/stu650
- Satyapal, S., Secrest, N. J., Ricci, C., Ellison, S. L., Rothberg, B., Blecha, L., et al. (2017). Buried AGNs in Advanced Mergers: Mid-infrared Color Selection as a Dual AGN Candidate Finder. *ApJ* 848, 126. doi:10.3847/1538-4357/aa88ca
- Schawinski, K., Koss, M., Berney, S., and Sartori, L. F. (2015). Active galactic nuclei flicker: an observational estimate of the duration of black hole growth phases of $\sim 10^5$ yr. *MNRAS* 451, 2517–2523. doi:10.1093/mnras/stv1136
- Schwartzman, E., Clarke, T. E., Nyland, K., Secrest, N. J., Pfeifle, R. W., Schmitt, H. R., et al. (2023). VaDAR: Varstrometry for Dual AGN using Radio interferometry. *arXiv e-prints*, arXiv:2306.13219doi:10.48550/arXiv.2306.13219
- Shen, Y., Chen, Y.-C., Hwang, H.-C., Liu, X., Zakamska, N., Oguri, M., et al. (2021). A hidden population of high-redshift double quasars unveiled by astrometry. *Nature Astronomy* 5, 569–574. doi:10.1038/s41550-021-01323-1
- Shen, Y., Hwang, H.-C., Zakamska, N., and Liu, X. (2019). Varstrometry for Off-nucleus and Dual Sub-Kpc AGN (VODKA): How Well Centered Are Low-z AGN? *ApJL* 885, L4. doi:10.3847/2041-8213/ab4b54
- Skilling, J. (2004). Nested sampling. *AIP Conference Proceedings* 735, 395. doi:10.1063/1.1835238
- Smith, K. L., Shields, G. A., Bonning, E. W., McMullen, C. C., Rosario, D. J., and Salvander, S. (2010). A Search for Binary Active Galactic Nuclei: Double-peaked [O III] AGNs in the Sloan Digital Sky Survey. *ApJ* 716, 866–877. doi:10.1088/0004-637X/716/1/866
- Toomre, A. and Toomre, J. (1972). Galactic Bridges and Tails. *ApJ* 178, 623–666. doi:10.1086/151823
- Torres-Albà, N., Iwasawa, K., Díaz-Santos, T., Charmandaris, V., Ricci, C., Chu, J. K., et al. (2018). C-GOALS. II. Chandra observations of the lower luminosity sample of nearby luminous infrared galaxies in GOALS. *A&A* 620, A140. doi:10.1051/0004-6361/201834105
- Van Wassenhove, S., Volonteri, M., Mayer, L., Dotti, M., Bellovary, J., and Callegari, S. (2012). Observability of Dual Active Galactic Nuclei in Merging Galaxies. *ApJL* 748, L7. doi:10.1088/2041-8205/748/1/L7
- Wang, J.-M., Chen, Y.-M., Hu, C., Mao, W.-M., Zhang, S., and Bian, W.-H. (2009). Active Galactic Nuclei with Double-Peaked Narrow Lines: Are they Dual Active Galactic Nuclei? *ApJL* 705, L76–L80. doi:10.1088/0004-637X/705/1/L76
- Weston, M. E., McIntosh, D. H., Brodwin, M., Mann, J., Cooper, A., McConnell, A., et al. (2017). Incidence of WISE -selected obscured AGNs in major mergers and interactions from the SDSS. *MNRAS* 464, 3882–3906. doi:10.1093/mnras/stw2620
- Yamada, S., Ueda, Y., Oda, S., Tanimoto, A., Imanishi, M., Terashima, Y., et al. (2018). Broadband X-Ray Spectral Analysis of the Double-nucleus Luminous Infrared Galaxy Mrk 463. *ApJ* 858, 106. doi:10.3847/1538-4357/aabacb
- Zhou, H., Wang, T., Zhang, X., Dong, X., and Li, C. (2004). Obscured Binary Quasar Cores in SDSS J104807.74+005543.5? *ApJL* 604, L33–L36. doi:10.1086/383310
- [Dataset] ZuHone, J. A., Vikhlinin, A., Tremblay, G. R., Randall, S. W., Andrade-Santos, F., and Bourdin, H. (2023). SOXS: Simulated Observations of X-ray Sources. Astrophysics Source Code Library, record ascl:2301.024